Experimental Studies of Flow-Structure Interactions in Blast/Shock-Driven Complex Flows

By

Parker Zieg

May, 2022

Director of Thesis: Dr. Yang Liu

Major Department: Engineering

ABSTRACT

Blast waves, which are generated by the sudden energy release in a finite space, are encountered in various situations. As the blast/shock waves propagate, any object in its path can be damaged by the combination of significant compression behind the shock front and the subsequent complex flow-structure interactions. Insufficient protection from blast loads has led to a significant loss of human lives and enormous structural damage and economic loss, highlighting the importance of developing effective blast/shock mitigation technologies. However, due to the lack of fundamental knowledge in the flow-structure interactions in various blast/shock conditions, the conventional methods of mitigating blast/shock have relied on the brutal use of various cladding rigid/soft materials where the coupling between the flow and structures is usually ignored. Challenges remain in understanding the complex flow-structure interactions driven by the rapidly-evolving nonlinear blast/shock waves. In this thesis, a series of experiments were carried out in the East Carolina University Advanced Blast Wave Simulator (ECU-ABWS) to characterize the flow-structure interactions (particularly the flow-airfoil interactions) under various blast/shock conditions. While the incident (side-on) pressures at multiple locations along the blast propagation were measured by using a temporally-resolved multi-point pressure sensing system, the time-evolutions of blast-airfoil interactions were also qualitatively revealed by using a high-speed Schlieren imaging system. A high-accuracy force/moment measurement system was also developed and used to determine the aerodynamic responses of the airfoil structure under various blast conditions. The understanding of these interactions allows for the further development of more efficient blast/shock mitigation techniques.

EXPERIMENTAL STUDIES OF FLOW-STRUCTURE INTERACTIONS IN BLAST/SHOCK-DRIVEN COMPLEX FLOWS

A Thesis

Presented to the Faculty of the Department of Engineering

East Carolina University

In Partial Fulfillment of the Requirements for the Degree

Masters of Science in Mechanical Engineering

By

Parker Zieg

May, 2022

Experimental Studies of Flow-Structure Interactions in Blast/Shock-Driven Complex Flows

By

Parker Zieg

APPROVED BY:

Director of Thesis _____

Yang Liu, Ph.D.

Committee Member _____

Yang Liu, Ph.D.

Committee Member _____

Teresa Ryan, Ph.D.

Committee Member _____

Zhen Zhu, Ph.D.

Chair of the Department of Engineering _____

Barbara Muller-Borer, Ph.D.

Dean of the Graduate School _____

Paul J. Gemperline, PhD

ACKNOWLEDGEMENTS

There are many people who have given a great deal of their time to help in this project. Thank you to Dr. Liu who has provided me with knowledge and guidance for the past few years. Thank you to Jim Menke who dedicated countless mornings and afternoons to helping supervise and assist in this project. Thank you to Andrew Wilson who has helped develop and maintain a variety of components needed to complete this project. Thank you to Dr. Ryan for providing me with knowledge, wisdom, and advice for the entirety of my time at ECU. Lastly, I would like to thank my parents and brother for their endless support and encouragement.

TABLE OF CONTENTS

LIST OF TABLES

LIST OF FIGURES

CHAPTER I. INTRODUCTION

A. Blasts, shocks, and their effects

Shock waves and blast waves have a great impact on their surroundings. While much of the physics that govern blasts and shocks are shared, there is one major difference: blasts are shock waves with unpredictable transient behavior. As a blast occurs, parameters including pressure, density and velocity reach maximum values and then decay to ambient. Shock waves in general are a result of a large difference in flow velocity producing a great amount of friction over the surfaces they contact.

There are several ways in which blasts and shocks may be formed. In general, a blast wave is the result of a sudden energy release. This energy release may come from the detonation of explosives or simply the rupture of a pressure vessel. One of the most practical ways in which a shock is formed is supersonic flight. Currently, there are a variety of vehicles that are capable of traveling well above the speed of sound including jets and missiles. In supersonic flight, air particles are unable to travel upstream and form a front ahead of the moving aircraft. These fronts form from collisions of molecules which can either result in a shock or an expansion wave. The formation of shocks results in greater surface pressure and temperature on the leading edges of the aircraft. As the transition towards hypersonic flight is taking place, the interactions between these high-speed flows and the structures encountering them is of great interest.

While shocks have a great impact on the external aerodynamics surfaces of aircrafts, they also interact with internal components such as compressors and turbines in jet engines. One such concern is related to the flutter of turbine propellors resulting from unsteady pressure distributions caused by shock formation [1]. Unsteady blade rotation and flutter increase the complexity of the flow-structure interaction and in turn impact the system as a whole. This

complexity increases for flows containing droplets and other particles. For any typical shock, the Rankine-Hugoniot relations may be used as a culmination of the conservation equations to relate physical properties for a jump across a shock wave; for a two-phase flow, the governing equations increase in complexity [2]. Because of the difficulties relating to the formulation of an experimental approach to understanding these complex interactions, numerical approaches are often used. Numerical investigations have been conducted to further understand such interactions, including the impact of these supersonic multi-phase flows on wall temperature [3].

When considering the complexity of a supersonic flow over a structure, it is often idealized that there are no additional external inputs into the system. In reality, there a variety of particles, dusts, and droplets that may interact with the flow as well. Adding additional inputs to such a system can result in large discrepancies between simulated, idealized flight conditions and the actual flight. Furthermore, the interaction between droplets and supersonic flows is pertinent to the spark ignition of fuel sprays [4]. Upon the contact between a droplet and a shock or blast, the interaction becomes multiphase, as air bubbles are introduced to the droplets. This phenomenon results in complexities within the fuel injection process. Similarly, when an external droplet impinges on the aircraft body, the aerodynamic properties of the aircraft will also be affected in a complex manner. When an aircraft is traveling at supersonic speeds, the maneuverability becomes greatly limited, meaning that any slight disruption in the expected aerodynamics can have major repercussions.

Several studies have been conducted to better understand the shock-droplet interactions [5-7]. Such studies investigate the breakup regime of the droplet, the breakup dynamics, and the droplet instabilities. A variety of complex phenomena dictate the shock droplet interactions including Richtmyer-Meshkov instability, Rayleigh-Taylor instability, and Kelvin Helmholtz

waves. It is possible to predict the breakup characteristics of a droplet by way of the Weber and Ohnesorge numbers.

While the formation of shock waves is predictable, sudden exposure to a blast wave is not. In many scenarios, blasts are formed by the detonation of explosives in military-related conditions. The impacts blast waves have had on humans, vehicles, and structures in the last century have been widespread. Although blasts are not limited to military conflicts, they may be easily weaponized for large-scale destruction. The direct impact of ΔP on the human body is shown in Table 1.

TABLE 1: Effects of overpressure on humans [8].

Peak Overpressure, Δp [psi]	**Impact on the human body**
2.39	Eardrum damage at 1% affected
2.80	Eardrum damage at 10% affected
5.00	Eardrum damage at 50% affected
6.29	Lung damage threshold
14.50	Fatal injuries at 1% affected
17.51	Fatal injuries at 10% affected
20.49	Fatal injuries at 50% affected
25.50	Fatal injuries at 90% affected
29.01	Fatal injuries at 99% affected

Apart from causing brain trauma to humans, blast waves from explosions have resulted in countless destroyed vehicles and buildings. For example, the Beirut explosion of 2020 resulted in $15 billion in damage, with hundreds of deaths and thousands of injuries. Large-scale blasts can travel hundreds of miles and pose a threat to not only vehicles and people on the ground, but also aircrafts. As blasts meet a structure of any sort, they are immediately reflected, but not without transferring momentum and energy to said structure. This sudden increase in momentum and energy may result in control system malfunction, a mechanical malfunction, or general deformation which would alter the aerodynamic properties of the aircraft and result in a crash.

B. UAV Dependence and potential threats

As drones become increasingly depended upon for the delivery of valuable payloads, there is a need to better understand the potential threats that a blast may pose on such vehicles. UAVs are frequently used for hazard detection and surveillance as well as for rescue operations [9]. Drones may also be used for the rapid transportation of blood products, organs, and other valuable materials [10, 11]. UAVs are also frequently used in combat [12]. There are several classifications of UAVs, or unmanned aerial systems (UAS), as recognized by the Department of Defense as shown in Table 2 [13].

TABLE 2: Joint UAS Groups.

UAS Category	Weight [lb.]	Altitude, AGL [ft]	Speed [knots]
1	< 20	<1,200	<100
2	21-55	<3,500	<250
3	<1,320	<18,000	<250
4	<1,320	<18,000	Any
5	>1,320	>18,000	Any

The groups of drones are determined by the weight, altitude above ground level (AGL) and speed and can also be broken into military and civilian groups. As there is a wide range of UAS groups and applications, there is a great interest in developing an understanding of the fluid dynamics and acoustics relating to these systems. In recent years, UAV technology progressed substantially, with a significant increase in payload capacities. As payload capabilities increase, the potential for using UAVs for human transportation may be realized; thus, a greater understanding for the interaction between blast, shocks and aircraft must be understood.

C. Approaches in Shock/Blast Studies

Due to the fact that blast waves and shocks are governed by the Rankine Hugoniot relations and many of the same physics apply to both, they can be investigated in a similar fashion. When considering a shock formed by supersonic flight, the shock is traveling with the aircraft, far above the speed of sound, just as a blast wave would. A variety of methods have been used to investigate the effects of blasts and shocks. Due to their destructive nature, much of the research being conducted is carried out computationally [14-19]. Recently, a large portion of the research being conducted is geared towards shock-shock interaction, shock-body interaction and shock-induced vortex formation. While the numerical approaches are capable of quickly and safely investigating such phenomena, it is essential to validate said phenomena with experimental data. Experimental approaches can involve the detonation of explosives, but are more commonly carried out in transonic, supersonic, and hyper sonic wind tunnels, with shock tubes, and with blast wave simulators [20-23].

While there are a variety of ways to generate a shock or blast, there are also several ways in which they are observed. Due to their supersonic speed, high-speed and high-fidelity equipment must be used for experimental approaches. There are several key features of a blast wave that are used to characterize their propagation including pressure, velocity, temperature, and morphology. In order to capture these elements, a wide range of methods have been developed. Generally, high-speed pressure sensors are used in nearly all experimental settings [24-27]. These pressure sensors are used to develop a pressure time history of the blast overpressure. Additionally, when analyzing the interaction between blasts and various structure, pressure sensitive paint has been found to be effective in analyzing surface pressure [28]. Alternately, methods to visualize blast and shock propagation include high-speed Schlieren

imaging and particle imaging velocimetry (PIV). In its most basic form, Schlieren imaging captures the density gradient off a blast making it visible – this is typically only a qualitative approach. However, methods for quantitative Schlieren imaging have also been developed [29,30]. Similarly, PIV is used to quantify the velocity field of high-speed phenomena [31-33]. Each of the approaches mentioned has its particular strengths and weaknesses relating to fidelity, reliability, and accuracy.

D. Blast/Shock mitigation techniques

A variety of approaches have been developed to mitigate the effects of blasts/shocks. In many of these approaches, the blast loading is the main parameter of interest, with the coupling between the flow and the structures being ignored. Approaches that have proven successful in reduction of the blast impact range from the use of soft materials for surfaces to developing water-filled walls. While the use of water-filled walls resulted in an 89% pressure reduction [48], when looking to apply blast mitigation techniques to an aerial vehicle, weight is a critical factor. The research shown in this study will ultimately be coupled with various blast mitigation techniques to evaluate their efficacy in an aerospace application.

When considering the formulation of the fluid structure interaction between a blast and a flexible structure, the loading scenario may be idealized as a single-degree-of-freedom system consisting of a load, spring, damper, and a surface of interest [49]. This idealized representation of the blast loading scenario proved to accurately determine the effects of aerodynamic damping for weak shocks. It is worth noting that the model here only remains valid for weak shocks, as the effects of compressibility become a concern for strong shocks [49].

One main area of research relating to blast mitigation is for the reduction of traumatic brain injury (TBI), which was the most prevalent military injury in Iraq and Afghanistan [50-52]. While several numerical models have been developed relating to TBI, others investigate current and potential combat helmet materials including polyurethane foam, highly viscoelastic polymers and polyurea. Generally, polyurea has been found to be one of the most effective materials for blast mitigation. One of the leading proposals for blast mitigation is that the layering of materials of decreasing densities would likely improve blast attenuation in existing helmets [52].

When looking towards effectively mitigating the impact of blasts relating to aerodynamic structure, surface coatings are one of the more prevalent approaches. Polyurea has shown to exhibit a range of mechanical properties from plastics to rubbers, making it a viable option for a surface coating. The material is comprised of a hard domain and a soft domain: the former lends itself to shock wave mitigation and the latter to ballistic protection. Retrofitting a steel plate with polyurea was found to greatly improve blast resistance, by way of reducing the overall deformation of the plate [53]. Furthermore, the material can be sprayed onto a surface of interest at sub-zero temperatures, greatly simplifying the application process. There is research of other similar materials, however, polyurea is currently the most widely accepted and readily available. The impact of polyurea on the aerodynamic performance of aerial vehicle components has yet to be investigated.

One novel approach to blast mitigation is by way of water droplet clouds. The multi-phase flow-droplet-structure-interaction becomes increasingly complex with the introduction of droplets. As mentioned in chapter 2, the characterization of droplet breakup and droplet-shock interactions is largely carried out experimentally, due to the complex nature of the phenomenon.

There are several simple factors that determine the level of attenuation achieved by droplet clouds: loading and particle size. While several studies have investigated the efficacy of various dusts to mitigate blast impacts [54], water droplets have been found to be the most effective due to their large heat capacity and latent heat of vaporization [55].

One study was conducted to evaluate the efficacy of water droplet clouds of various size droplets to reduce the measured overpressure at several locations through a shock tube. It was found that the largest droplet (500 μm) greatly reduces the overpressure at each of the three stations. While this study does not determine an optimal droplet size with respect to the expected overpressure, it does confirm that water droplets are capable of reducing the overall blast pressure at various locations from the source. This conclusion has little impact on mitigating blast impacts for aerial vehicles, however it was major implications for shock interaction sin supersonic vehicles. In order to better understand the relationship between theses droplets and shocks/blasts, it is necessary to investigate a greater range of droplet sizes across a greater range of overpressure values. Furthermore, coupling this multi-phase flow with a structure will provide insight into using water droplet clouds for blast mitigation for various structures.

E. Description of the Present Study

This research attempts to provide a greater understanding of the relationship between shocks and blasts and their surroundings. Particularly, this research aims to develop a relationship between blast magnitude and airfoil aerodynamics. This investigation aims to answer the following questions:

- How can blasts/shocks be produced and generated?
  - Can repeatable blast overpressures be generated?

- How does blast morphology vary with blast overpressure?

- How do blasts/shocks interact with an airfoil structure?
  - What are the transient flow-airfoil interactions driven by blasts/shocks?
  - Does blast overpressure change the flow-structure interaction morphology?
  - Does blast overpressure have a particular relationship with airfoil lift and drag?

First, it is necessary to gain an understanding of the physical laws that govern blast/shock propagation. Here, the second chapter aims to provide a foundation of blast/shock physics that will allow for a further understanding of their behaviors. In order to investigate shocks/blasts, an advanced blast wave simulator is used to generate blasts, which can also represent a shock wave. It is essential to first fully characterize the blasts generated by the simulator to later understand their interactions with the airfoil structure. This is done by using a high-speed measurement system consisting of pressure sensors and a Schlieren imaging system. This measurement system allows for both the visualization and the quantification of various blasts. This blast simulator is capable of producing a wide range of overpressures, and this measurement system will determine the repeatability of these pressures. Chapter 3 details the investigation of the advanced blast wave simulator as well as the measurement system.

In order to develop an understanding of the interaction between blasts/shock and an aerodynamic structure a NACA 0012 airfoil model was used in this thesis. Schlieren imaging as well as a temporally resolved force sensing system were used for this investigation. These systems provided insight into the flow-structure interaction morphology as well as the physical impact blasts/shock have on the airfoil lift and drag. A detailed description of this study will be provided in Chapter 4.

In total, this thesis begins with understanding blast/shock properties, then using this understanding to tune an advanced blast wave simulator for the investigation of the fluid-structure interactions, i.e., flow-airfoil interactions, driven by shocks/blasts, then finally providing some insights for developing blast/shock mitigation techniques. This work aims to advance the general understanding of blasts/shocks and their interactions with their surroundings in an attempt to provide a foothold for the development of more effective blast/shock mitigation technologies.

CHAPTER II. BLAST/SHOCK PHYSICS

A. Blast and shock generation

There are several experimental methods that are used to produce blasts and shocks. The first and most obvious method includes the detonation of explosive charges. The use of explosive charges represents the most robust experimental approach, as such studies consider environmental factors. As the use of explosive charges comes with safety concerns, large open fields with proper blast barriers are required for the detonation of any sort of explosives. Additionally, proper oversight and training are required to handle and operate explosives. Generally, the smaller scale an explosive is, the more care is required to handle it. Each explosive has a critical diameter which represents the minimum size for detonation [34]. Table 3 displays the critical diameters for several common explosives [35].

TABLE 3: Explosives and their critical diameter [35].

Explosive	Critical Diameter (cm)
PETN	0.02
PBX-9404	0.118
RDX	0.2
TNT, Pressed	0.26
Octol	0.64
Pentolite	0.67

Many studies utilize explosive charges to generate blasts. One such study used explosives to analyze the impact blast waves have on UAV aerodynamic properties, the ability of directed acoustic energy to disrupt a UAVs flight has been investigated [36]. In this study, C-4 was detonated four to ten feet from a DJI Phantom 4 Pro quadracopter, with the goal being to analyze the ability to disable or down a drone flying in undesired airspace. The trials were evaluated on a

pass-fail basis and did not measure the aerodynamic properties of the drone [36]. The minimum ΔP that was found to disable the drone was 24.9 psi.

A more common and idealized approach to investigating blasts and shock is the use of shock tubes or other blast wave simulators. In general, a shock tube consists of three sections: a driver section, a driven section, and a test section. The main requirement of such a configuration is that the volume of the driver section must be much smaller than the driven section; this allows for the production of a rarefaction wave [34]. The term "shock tube" encompasses several blast generation techniques. While shock tubes can range in size, they can also vary in shock production techniques. One of the more common techniques is to use the detonation of a high explosive charge in the driver section. This method mitigates the risk associated with the free-air propagation of larger-scale explosive charges. Furthermore, the use of smaller-scale high explosives is easily scalable by the cube root of the charge size [34]. Electrical sparks, the release of compressed gas and pistons can also be used to generate shocks in the driver section of a shock tube.

B. East Carolina University Advanced Blast Wave Simulator

While access to explosives of any sort is limited, the access to large-scale blast simulators is as well. East Carolina University is home to an Advanced Blast Wave Simulator (ABWS), which utilizes a compressed gas driver section. The ABWS is shown in Figure 1.

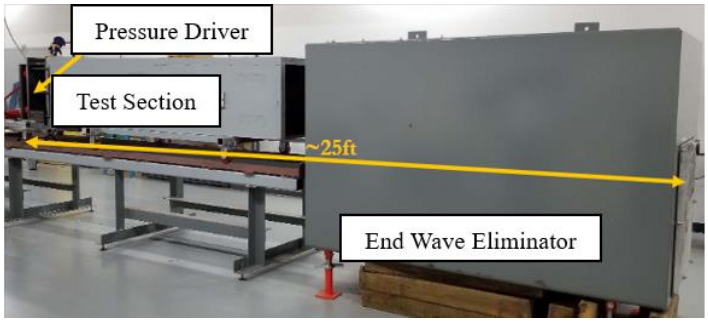

FIGURE 1: East Carolina Advanced Blast Wave Simulator.

As shown in Figure 1, there are three main sections of the ABWS: the pressure driver, the test section, and the end wave eliminator. The test section of the chamber has a cross-sectional area of 2 ft × 2 ft. In order to produce a blast, a biaxially-oriented polyethylene terephthalate (Mylar) membrane is placed between the pressure driver and the test section. An air compressor delivers pressurized air to the pressure driver through a network of conduit, controlled from a safe distance, until the pressure in the driver section is great enough to rupture the Mylar membrane. Upon rupture, the sudden energy release results in a blast wave being sent through the test section and into the end wave eliminator. The ABWS can generate blasts of up to 16 psi.

C. Problem formulation and governing equations

Generally, any sort of acoustic wave propagates spherically away from the source. Because of the difficulties that arise with spherical waves, they are often idealized as plane waves. When looking at a small section of a wave sufficiently far away from the source, the wave begins to physically become a plane wave as shown in Figure 2.

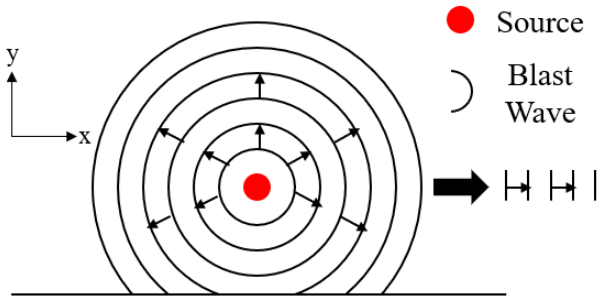

FIGURE 2: Blast wave propagation idealized as a plane wave.

A typical sound wave is in part characterized by the acoustic pressure which oscillates about the ambient pressure and ultimately decays back to ambient. However, when the pressure amplitude of such waves increases, sound waves become unable to release energy at the rate it is deposited [37]. In turn, the surrounding gas is compressed, increasing the local temperature and ultimately, the local speed of sound. The relationship between temperature and the local speed of sound is given by Equation 1 as

$$c = \sqrt{\gamma RT}\,, \tag{1}$$

where γ is the heat capacity ratio, R is the ideal gas constant and T is the absolute temperature [38]. Thus, a sudden release of a large amount of energy results in the surrounding air traveling supersonically away from the source, creating a sonic boom, and propelling surrounding particles and debris at high velocities. The leading front of a blast wave may be described as the shock front of the blast and can be characterized by the maximum pressure it reaches, or the peak overpressure, ΔP, which is measured with respect to the ambient pressure as shown in Equation 2.

$$\Delta P = P - P_0 \tag{2}$$

In general, such acoustic phenomena may be represented as Friedlander waveforms, describing the pressure as a function of time, and following Equation 3 as

$$P(t) = \Delta P e^{-\frac{t}{t^*}}\left(1 - \frac{t}{t^*}\right) \tag{3}$$

where t^* is the initial time at which the pressure crosses the x-axis before becoming negative as shown in Figure 3.

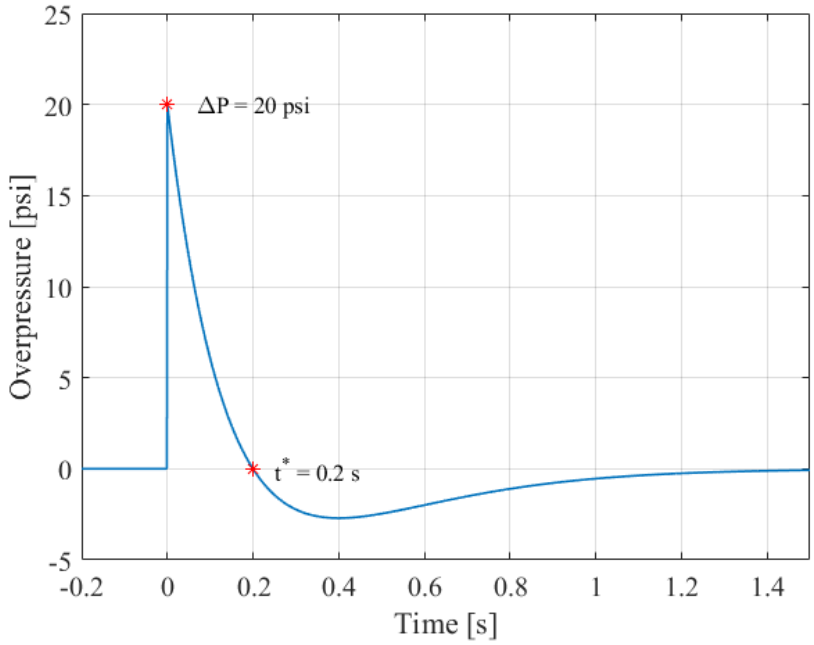

FIGURE 3: Friedlander waveform.

In agreement with the definition of a blast wave, the Friedlander waveform describes the exponential decay that occurs immediately after the compressed gas reaches its maximum density, pressure, and velocity. Although this waveform accurately represents the pressure magnitude over time, it does not account for the higher frequency sinusoidal pressure oscillations about the ambient. In addition to using measuring the overpressure, the Friedlander waveform

can be used to determine the impulse of a blast. Referring to Figure 3, the impulse is the area under the curve for the positive overpressure duration of the waveform.

In addition to analyzing the pressure generated by a blast wave, there are several other parameters of interest. The Rankine-Hugoniot relations describe the conservation of mass, momentum, and energy as well as the equation of state across a shock front. The following relations are given for one-dimensional, adiabatic normal shock with unit cross-sectional area as shown in Figure 4.

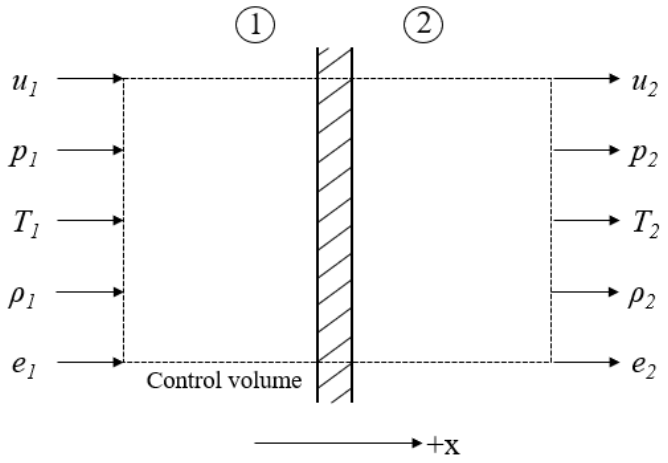

FIGURE 4: Rectangular control volume for one-dimensional flow [38].

The conservation of mass across the shock front is given by Equation 4 as

$$\rho_1 u_1 = \rho_2 u_2. \tag{4}$$

The conservation of momentum across a shock front is given by Equation 5 as

$$p_1 + \rho_1 u_1^2 = p_2 + \rho_2 u_2^2. \tag{5}$$

The conservation of energy across a shock front is given by Equation 6 as

$$h_1 + \frac{u_1^2}{2} = h_2 + \frac{u_2^2}{2} \tag{6}$$

where *h* is the enthalpy on either side of the shock wave, given by Equation 7 as

$$h = e + \frac{p}{\rho} \tag{7}$$

For a moving shock wave, the velocity of the gas ahead of the wave may be defined as *W* and the velocity of the fluid behind the wave is given by Equation 8 as

$$W - u_p = gas\ velocity\ behind\ the\ shock\ wave \tag{8}$$

Where u_p is the mass motion induced by a moving shock wave. Then for a moving normal shock wave, the conservation of mass, momentum and energy become Equations 9, 10 and 11, respectively.

$$\rho_1 W = \rho_2 (W - u_p) \tag{9}$$

$$p_1 + \rho_1 W^2 = p_2 + \rho_2 (W - u_p)^2 \tag{10}$$

$$h_1 + \frac{W^2}{2} = h_2 + \frac{(W - u_p)^2}{2} \tag{11}$$

Then, Equation 9 may be rearranged to provide Equation 12 as

$$W - u_p = W \frac{\rho_1}{\rho_2}, \tag{12}$$

which can then be substituted into Equation 10 to give Equation 13 as

$$p_1 + \rho_1 W^2 = p_2 + \rho_2 W^2 \left(\frac{\rho_1}{\rho_2}\right)^2. \tag{13}$$

This expression may be rearranged to yield Equation 14 as

$$W^2 = \frac{p_2 - p_1}{\rho_2 - \rho_1}\left(\frac{\rho_2}{\rho_1}\right) \tag{14}$$

Solving the continuity equation for *W* gives Equation 15 as

$$W = \left(W - u_p\right)\frac{\rho_2}{\rho_1} \tag{15}$$

Substituting Equation 15 into Equation 14 gives Equation 16.

$$\left(W - u_p\right)^2 = \frac{p_2 - p_1}{\rho_2 - \rho_1}\left(\frac{\rho_1}{\rho_2}\right) \tag{16}$$

Finally, substituting Equation 14 and 16 into Equation the energy equation and using the definition of enthalpy, the Hugoniot equation may be given by Equation 17 [39].

$$e_2 - e_1 = \frac{p_1 + p_1}{2}(v_1 - v_2). \tag{17}$$

For calorically perfect gasses, several of the above expressions may be simplified. The magnitude of material fluid velocity of the shock front may be given by Equation 18 as

$$u = \frac{\Delta P}{\gamma P_0}\frac{C_0}{\left(1 + \frac{[\gamma+1]\Delta P}{2\gamma P_0}\right)^{1/2}} \tag{18}$$

where C_0 is the ambient speed of sound, γ is heat capacity ratio, and P_0 is the ambient pressure [40]. This expression simplifies to Equation 19 for a heat capacity ratio of 1.4.

$$u = \frac{5\Delta P}{7P_0}\frac{C_0}{\left(1 + \frac{6\Delta P}{7P_0}\right)^{1/2}}. \tag{19}$$

Alternately, the magnitude of the shock velocity is given be Equation 20 as

$$U = C_0\left(1 + \frac{[\gamma+1]\Delta P}{2\gamma P_0}\right)^{1/2}, \tag{20}$$

which for a heat capacity ratio of 1.4 can be reduced to Equation 21 as

$$U = C_0\left(1 + \frac{6\Delta P}{7P_0}\right)^{1/2}, \tag{21}$$

Lastly, the temperature of the shock front can be given by Equation 21 as

$$\frac{T}{T_0} = \frac{2\gamma + (\gamma - 1)\frac{\Delta P}{P_0}}{2\gamma + (\gamma + 1)\frac{\Delta P}{P_0}}\left(1 + \frac{\Delta P}{P_0}\right), \tag{21}$$

which also may be simplified for a heat capacity ratio of 1.4 to Equation 22 [40].

$$\frac{T}{T_0} = \frac{7 + \frac{\Delta P}{P_0}}{7 + 6\frac{\Delta P}{P_0}}\left(1 + \frac{\Delta P}{P_0}\right) \tag{22}$$

While numerically representing the propagation of shocks and blasts is not a simple task, the interaction between such waves and their surroundings increases in complexity. In general, loading due to a blast is impulse loading. General expressions can be given for the reflected pressure of a blast encountering a surface normal to the propagation. However, for many aerodynamic structures, the geometries are far more complex than a flat plane. The pressure realized by a structure is a function of the reflected overpressure, ΔP_r, which for a heat capacity ratio of 1.4 is given by Equation 23 as

$$\Delta P_r = 2\Delta P\left(\frac{7 + 4\Delta P/P_0}{7 + \Delta P/P_0}\right) \tag{23}$$

Then, the reflection factor is simply the ratio of the reflected pressure to the incident overpressure. Again, this relation only holds true for surfaces normal to blast propagation [41]. In the case of a complex geometry (i.e., non-wedge, non-cone, non-planar), there is no concrete way to solve for a pressure load. For such problems, researchers rely on computational models and experimental data to predict pressure loads on various structure. However, for many geometries, there is tabulated data that agrees well with the theoretical models [42].

When a shock or blast encounters a structure, it is immediately reflected. However, upon contact with a structure, energy and momentum are imparted from the blast wave to the structure. In the case of the surface being non-perpendicular to the direction of shock or blast propagation, there will also be a considerable amount of friction on the surface. In high Reynolds number flows, a thin boundary layer forms at the surface of the structure. In any flow, there is a level of skin friction that must be accounted for. For fully turbulent flows, Equation 24 defines the skin friction coefficient as [43]

$$C_{f_{turb}} = \frac{0.455}{(\log_{10} Re)^{2.58}} \tag{24}$$

Where *Re* is the Reynolds number. However, this expression does not take compressibility into account. Because air is a compressible fluid factor plays a large role in supersonic flows, it needs to be considered as given by Equation 25 as

$$C_{f_{turb}} = \frac{0.455}{(\log_{10} Re)^{2.58}(1+0.144M^2)^{0.65}} \tag{25}$$

Where *M* is the Mach number of the flow. In addition, flow separation can also occur, greatly altering the flow state at the structure surface. The drastic increase in skin friction lends itself to an increase in wall temperature, which for a flat plate can be given by Equation 26 [44] as

$$T_{aw} = T_0^* \left(1 + r\frac{\gamma-1}{2}M^2\right)\left(1 + \frac{\gamma-1}{2}M^2\right) \approx \begin{cases} T_0^*, & M \ll 1 \\ rT_0^*, & M \gg 1 \end{cases} \tag{26}$$

Where T^*_0 is the stagnation temperature of the flow, γ is the heat capacity ratio and *r* is factor dependent on several parameters of the flow and geometry. In many cases, these phenomena are predictable only through computational approaches rather than a simple analytic approach. Furthermore, as the flow increases from supersonic to hypersonic, these parameters continue to increase in complexity.

D. Shock-droplet interaction

In a real-world environment, supersonic vehicles are likely to encounter droplets and particles in the air. As the current technology development has largely shifted towards the development of hypersonic vehicles, the interaction between shock waves and droplets has as well. Because of the complex nature of such multi-phase flows, the current research is largely experimental, attempting to develop predictive computational models.

There are a variety of parameters to consider when predicting the interaction between supersonic flows and droplets. The first two parameters to consider are the Weber and Ohnesorge numbers given by Equations 27 and 28, respectively [45].

$$We = \frac{\rho V_i^2 D_i}{\sigma} \tag{27}$$

$$Oh = \frac{\mu}{\sqrt{\rho \sigma D_i}} \tag{28}$$

Where σ is the surface tension of the air-liquid interface, D_i is the initial droplet diameter, ρ and V_i are the density and velocity of the air post-shock, and μ is the dynamic viscosity. These parameters can be used to predict the breakup regime of a droplet.

While the droplet breakup regime is predictable across a variety of Ohnesorge numbers, the interaction between the droplets and surfaces is less predictable. The impingement of a droplet on an aerodynamic structure at supersonic speeds can greatly alter the flight conditions. An initial step to understanding the relationship between the droplet-structure interaction is to first understand the relationship fully between shocks/blasts and aerodynamic structures.

CHAPTER III. CHARACTERIZATION OF ECU ABWS

A. Schlieren imaging and pressure sensing system

Despite the blast measurement system being synchronized and controlled by a central computer, it may be broken into two parts, the first of which is the temporally resolved pressure sensing system. Like the previous study, a PCB Piezotronics pressure sensor (P/N 102B15) is mounted inside the test chamber of the ABWS. The electrical signal produced by the pressure sensor is processed using a PCB Piezotronics Signal Conditioner. The resulting signal is then connected to a National Instruments USB-6211 DAQ. The DAQ is controlled by NI DAQ Express on a central CPU and data acquisition is triggered by a BNC Digital Delay / Pulse Generator. In order to process the pressure time history, MATLAB is used.

In addition to the pressure sensing system, a visualization system in the form of high-speed Schlieren imaging is used. Here, two Edmunds optics aluminized first-surface, six-inch diameter spherical mirrors are used. The mirrors have a focal length of 60 in. Referring to Figure 6, this means that the first mirror must be 60 in. from the light source and the resulting focused beam occurs 60 in. from the second mirror. Due to the physical-optic laws that govern Schlieren imaging, the distance between the two spherical mirrors is variable, allowing the mirrors to be placed on either side of the ABWS test section. Thus, the side plates of the ABWS have been replaced with plexiglass plates that allow the refracted light to travel from one side of the chamber to the other.

Here, a Texas Instruments DLP Lightcrafter 4500 projector is used as the light source. The projector is set to cast a plane white image, which is brighter than a typical light source. To capture the Schlieren image, a Photron FASTCAM Mini UX high-speed camera is used. In

general, the camera is set to record at 12,500 frames per second (FPS), with a shutter speed of 1/360,000s. The camera is controlled by the central computer and is also triggered by the BNC Digital Delay / Pulse Generator. The resulting images are also processed using MATLAB. Because both the high-speed camera and pressure sensors are connected to the pulse generator, they are synchronized. The entire visualization and pressure sensing schematic is shown in Figure 5.

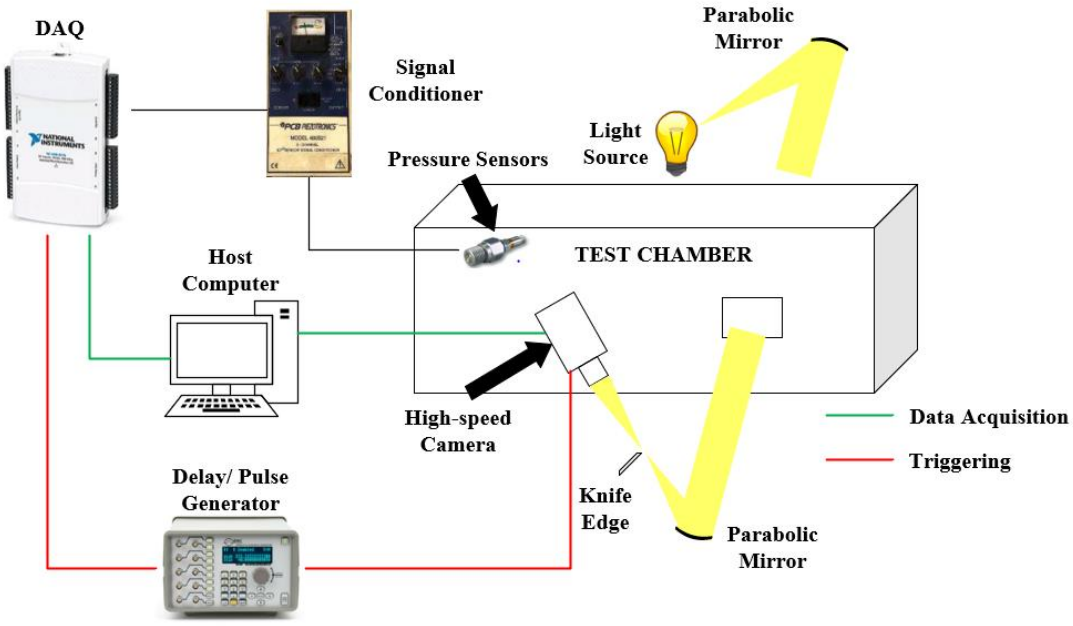

FIGURE 5: Full ABWS pressure sensing and visualization system.

In order to produce clear images of the blast waves, an image processing method has been developed. The raw image series are compiled into a MATLAB workspace and the image files are converted into single-precision data tables. The resulting tables contain light intensity data for each pixel of the image. The images are cropped by removing the excess rows and columns of the data tables. For each series, an image is captured prior to the blast wave entering the frame – this image may be considered a "background only" image. For the following images

that include the blast waves, the background only light intensity data is subtracted to remove any nonuniformities that result from dust or other debris.

B. Initial blast overpressure study

It was essential to confirm that the peak overpressures were obtainable and repeatable in the ABWS. Here, an initial study was conducted to develop both a relationship between the membrane thickness and overpressure as well as the burst pressure and the overpressure. The burst pressure represents the maximum pressure reached in the driver section of the ABWS prior to membrane rupture. For the purpose of this study, a total of eight membrane thicknesses were be used to evaluate the relationship between membrane thickness and the resultant overpressure, i.e., 0.001 in, 0.002 in, 0.003 in, 0.004 in, 0.005 in, 0.007 in, 0.010 in and 0.014 in. Five trials were recorded for each thickness and sample pressure time histories are shown for each thickness in Figure 6.

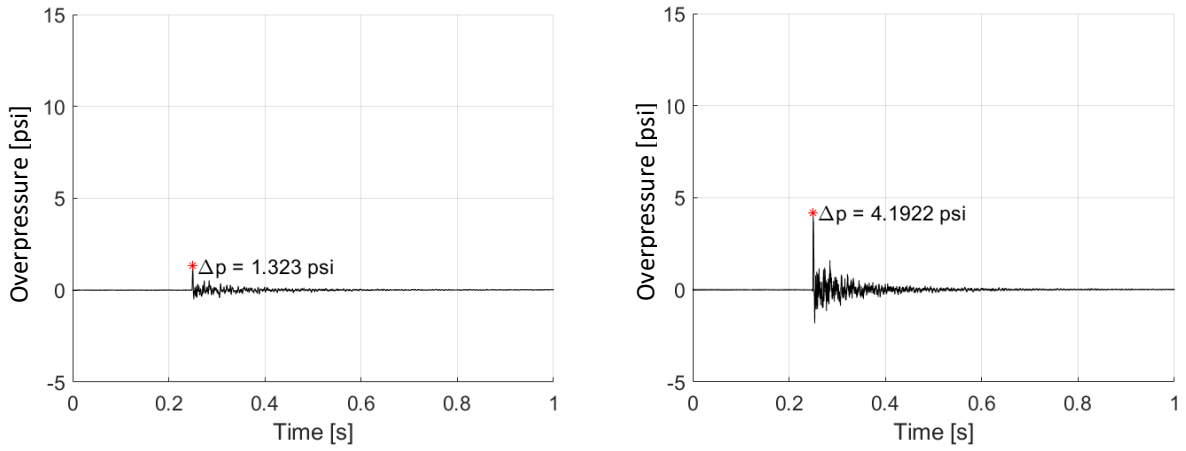

A. **B.**

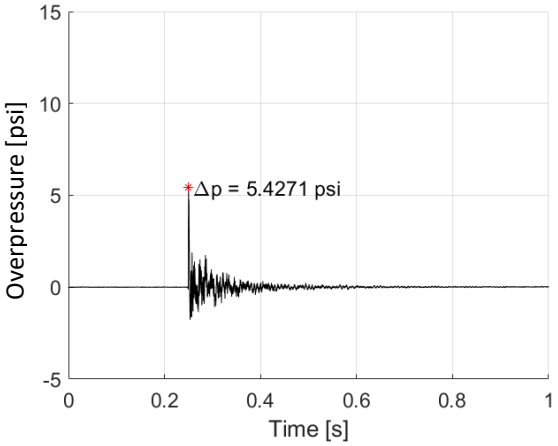
Δp = 5.4271 psi
Overpressure [psi]
Time [s]

C.

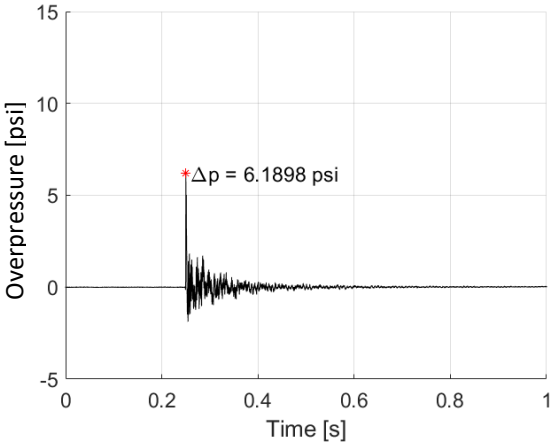
Δp = 6.1898 psi
Overpressure [psi]
Time [s]

D.

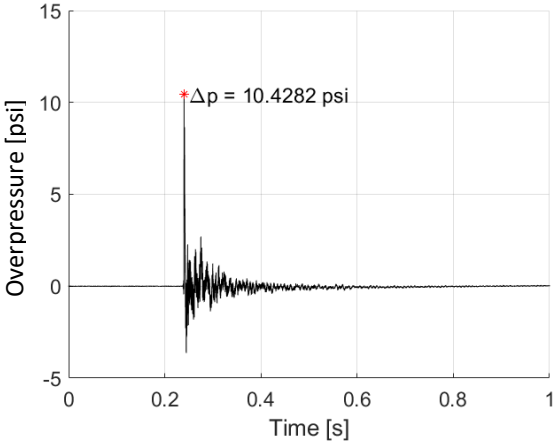
Δp = 10.4282 psi
Overpressure [psi]
Time [s]

E.

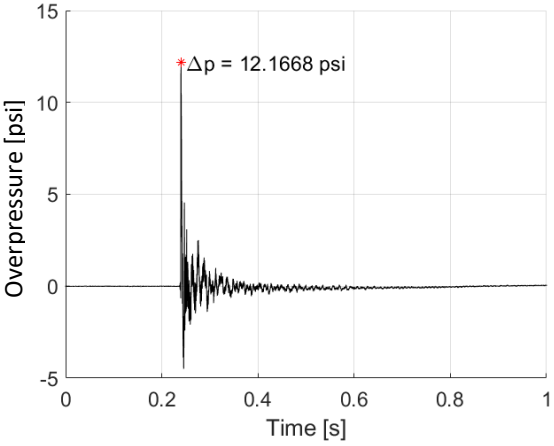
Δp = 12.1668 psi
Overpressure [psi]
Time [s]

F.

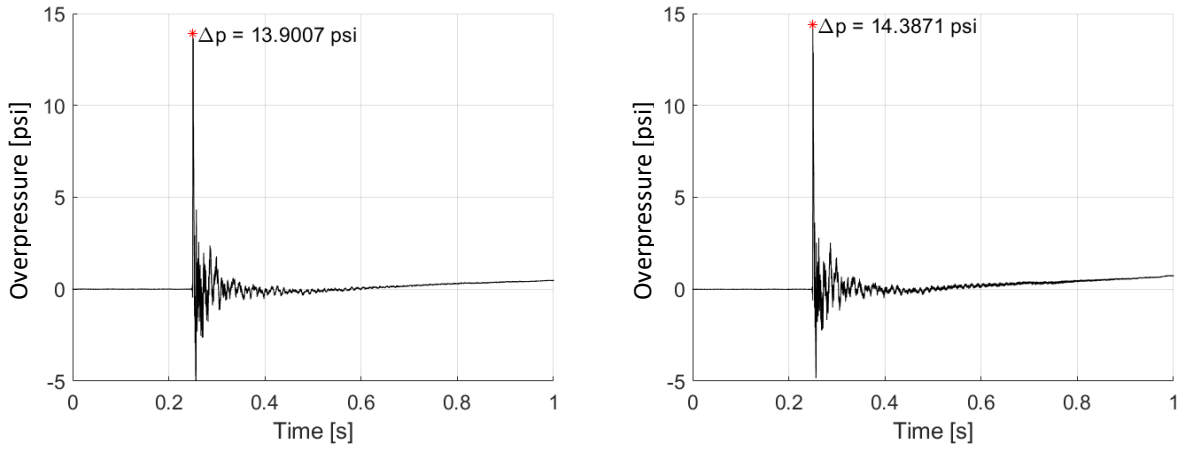

G. **H.**

FIGURE 6: Pressure time histories for membranes **A.** 0.001 in, **B.** 0.002 in, **C.** 0.003 in, **D.** 0.004 in, **E.** 0.005 in, **F.** 0.007 in, **G.** 0.010 in, **H.** 0.014 in. thick

When measuring the pressure time history of a blast wave using this experimental design, the triggering of data acquisition is manual. Because the membranes vary in thickness, the time the membranes take to rupture also varies. As a result, the peak overpressures are not synchronized; thus, the raw data has been post-processed to synchronize each series. When larger membranes are used, there is additional vibration in the chamber, resulting in the pressure rising above ambient as seen in Figure 7H. Although there are significant differences between the pressure of each membrane thickness, the settling time for each trail is roughly the same, at about 0.22 s.

As mentioned, five trials were conducted for each membrane thickness. Because the peak overpressure of each trial is the only parameter of interest here, it is not necessary to analyze each series, but rather just ΔP. The resulting ΔP values are plotted as a function of membrane thickness for all of the trials in Figure 7.

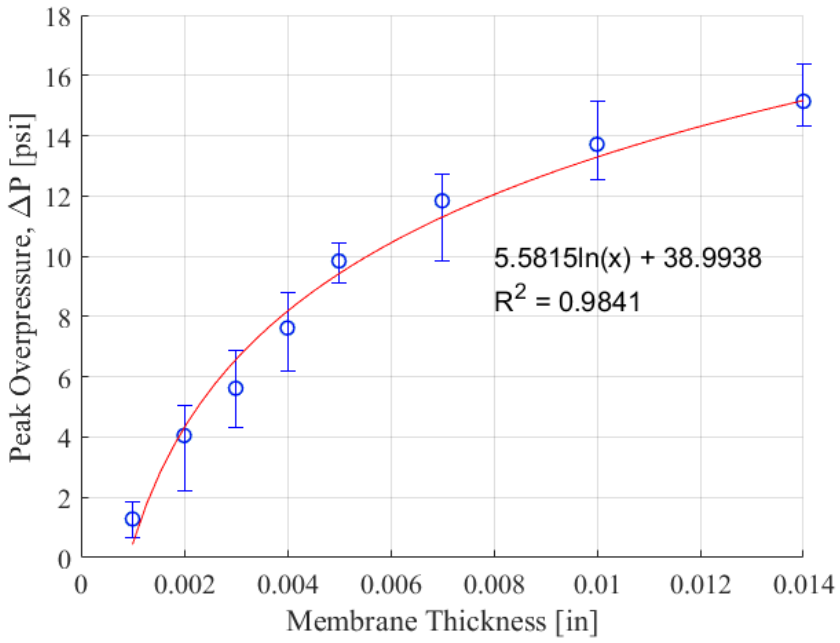

FIGURE 7: *ΔP* plotted as a function of membrane thickness.

As shown by the error bars in the above figure, each membrane thickness has a range of peak overpressures that it may produce. A curve fit was carried out for the average pressure of each membrane and the relationship between membrane thickness and *ΔP* was found to be logarithmic. Additionally, the coefficient of determination, R^2, was calculated as 0.9841 which signifies a good correlation. The previous study conducted to determine a relationship between the membrane thickness and *ΔP* resulted in a linear relationship [47]. The result here varies due to the increased number of membranes used. Without having smaller increments of membrane thickness, the relationship between membrane thickness and *ΔP* appears linear. However, despite the clear logarithmic relationship shown, there is not a good physical reasoning to explain this phenomenon.

In an attempt to develop linear relationship between the varying membrane thickness and the overpressure, the burst pressure-overpressure relationship was investigated. A digital

pressure gauge was mounted to the driver section of the blast wave simulator. The gauge was set to record only the peak pressure measured, which in this case is the burst pressure. For five trials of each membrane thickness the burst pressure and corresponding peak overpressure were recorded. Figure 8 shows the overpressure plotted as a function of burst pressure for each individual trial.

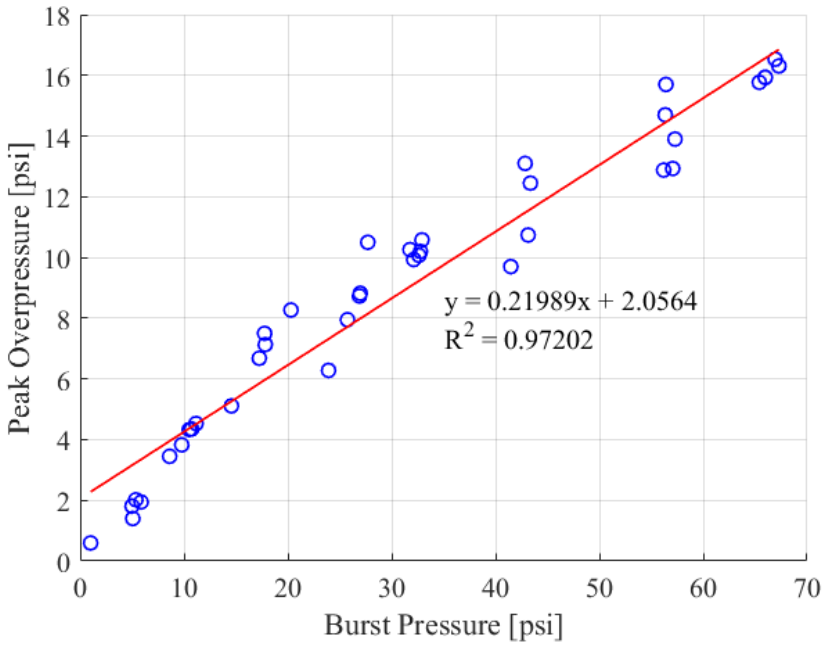

FIGURE 8: Peak overpressure plotted as a function of burst pressure for my membranes 0.001 in, 0.002 in, 0.003 in, 0.004 in, 0.005 in, 0.007 in, 0.010 in and 0.014 in thick.

Figure 8 shows a linear relationship between the peak overpressure and burst pressure as well as the representative regression line. The correlation coefficient of 0.9702 shows good agreement between the regression line and the collected data. A linear relationship for a wide range of membrane thicknesses and overpressures indicates that the ABWS is capable of producing predictable and repeatable overpressure values for the investigation of blasts of varying magnitude.

C. Initial shock front velocity study

In addition to measuring the pressure of each blast, the velocities of the blasts were computed using Equation 21:

$$U = C_0 \left(1 + \frac{6\Delta P}{7P_0}\right)^{1/2}, \tag{21}$$

Furthermore, the resulting mac numbers were computed using Equation 29 as

$$M = U/C_0 \tag{29}$$

Using these relations, the shock front velocities and shock front Mach numbers are plotted as a function of burst pressure in Figure 9.

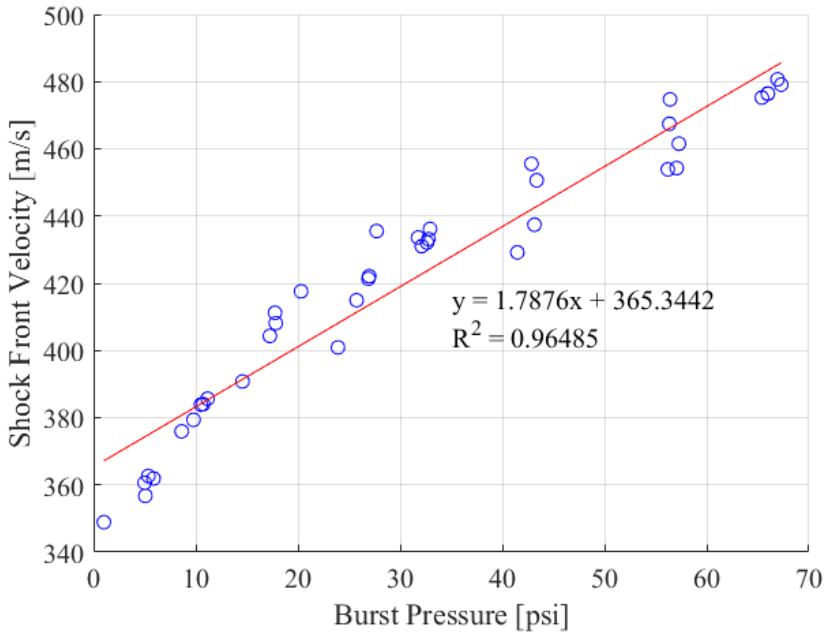

A.

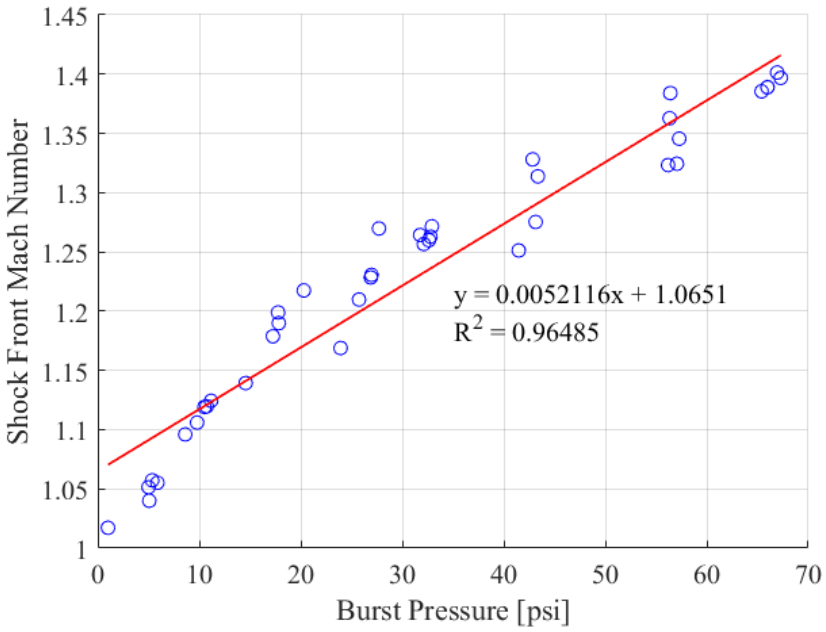

B.

FIGURE 9: Shock front velocity and shock front Mach number plotted as function of burst pressure.

As the figure shows, the linear relationship is the same as for burst pressure-overpressure; this is because the velocity is dependent on the overpressure. Again, there is good agreement between the linear regression line and the recorded data as reflected by the correlation coefficient of 0.9646 for both figures.

D. Initial Schlieren imaging of blast waves

In addition to quantifying each blast, the visualization of the blasts was carried out as well. The Schlieren imaging system described above was used to qualitatively display the density gradient within the test section of the ABWS. An initial study was conducted to determine the optimum shutter speed, frame rate and resolution for the high-speed camera. Because of the triggering system used, the camera stores 3 seconds prior to triggering as well as 3 seconds

afterwards. Because the camera has limited storage, as the frame rate increases, i.e., consecutive frames have shorter intervals, the resolution decreases. Thus, the maximum frame rate that allowed for a resolution that fully displayed the blast propagation was determined to be 12,500 FPS. Figure 10 shows the Schlieren image series for each membrane thickness.

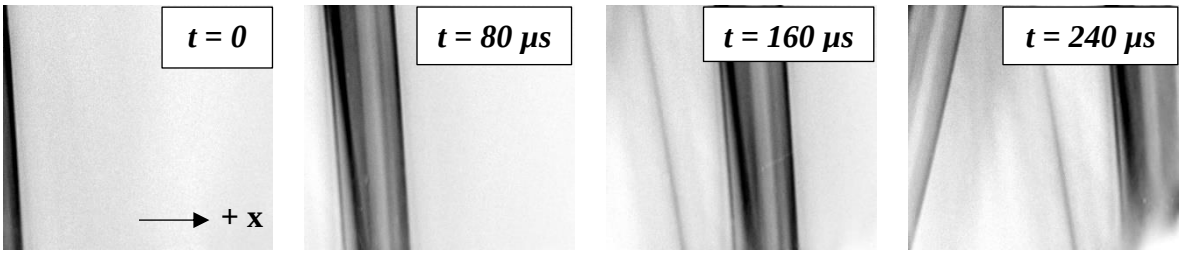

A.

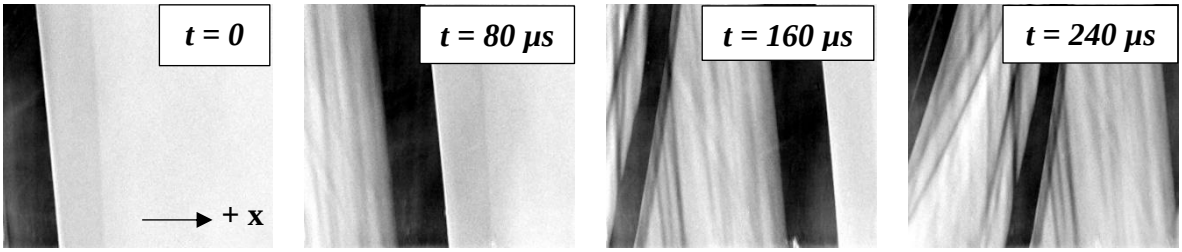

B.

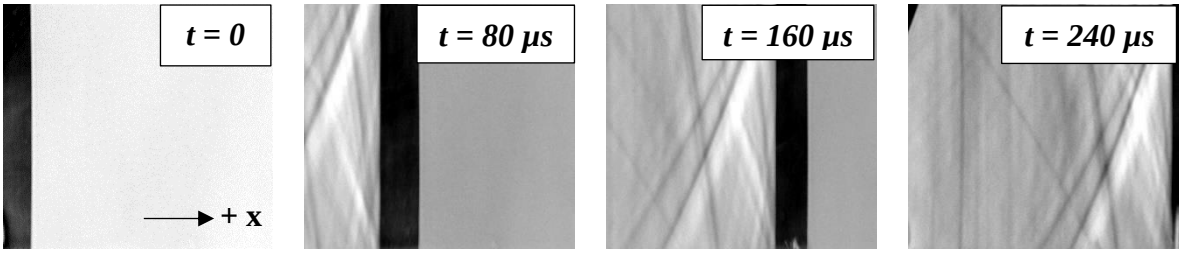

C.

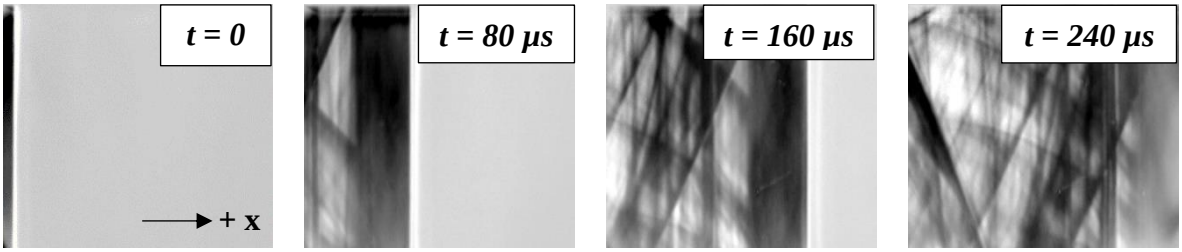

D.

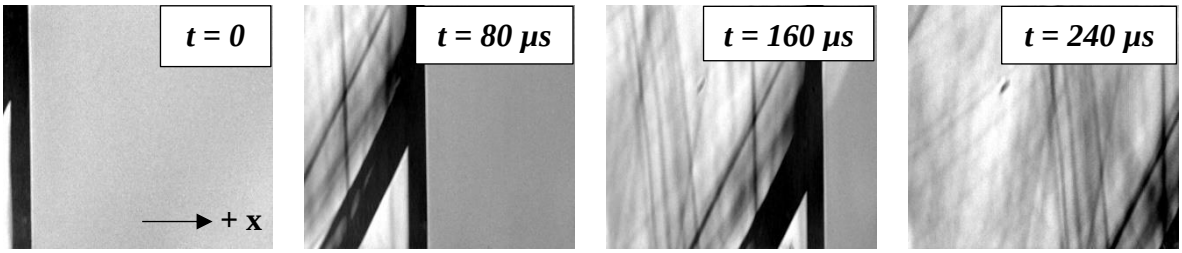

E.

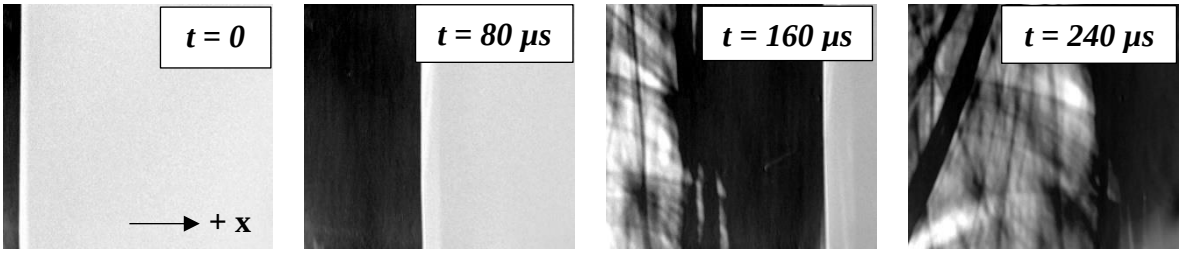

F.

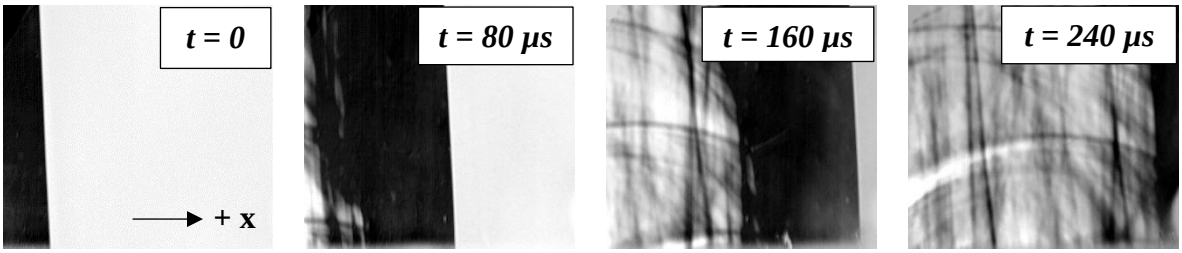

G.

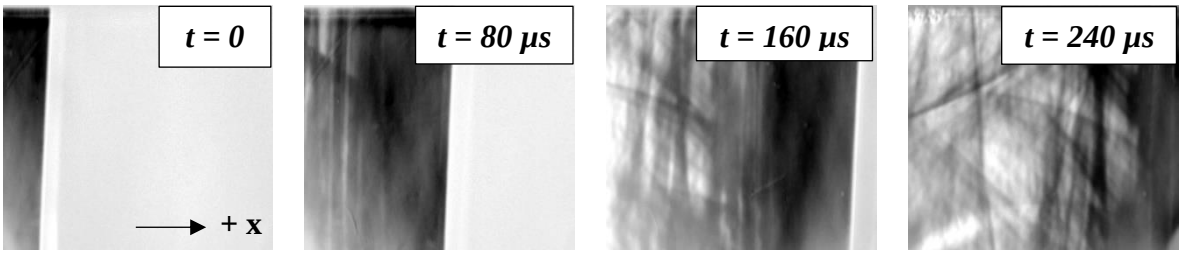

H.

FIGURE 10: Schlieren image series for each membranes **A.** 0.001 in, **B.** 0.002 in, **C.** 0.003 in, **D.** 0.004 in, **E.** 0.005 in, **F.** 0.007 in, **G.** 0.010 in, **H.** 0.014 in. thick.

As shown in the above figure, as the overpressure increases, as does the turbulence within the test chamber. In Figure 10A, a thin shock front can be seen propagating with minimal turbulence behind it. Moving to Figures 10B and 10C, the shock front begins to become more

defined and increase in turbulence. This continues up until Figure 10H where the shock front is the largest and most defined and the turbulence is at a maximum. The turbulence seen in the images is a result of small reflections off the test section walls. If the image series were to continue, the shock front would be seen retuning the opposite direction as a reflection. The end section of the ABWS is designed to absorb a large amount of the blast energy and ultimately fully dissipates the blast after several reflections.

The initial studies of pressure measurement and Schlieren imaging show that the ABWS is capable of producing repeatable overpressure values that can be clearly visualized. Having developed a synchronized pressure and imaging system, the ABWS can be used for further investigation of the interactions between blasts and aerodynamic components.

E. Shock front tracking

In an attempt to gain quantitative information from the Schlieren image series, a wavefront tracking method was developed. In order to calculate the velocity of the wave, Equation 30 is first used to develop a relationship, Δx, between a known distance between two points on the image, and the number of pixels between the two points in the image data. This is shown as

$$\Delta x = \frac{x}{pix_{x2} - pix_{x1}} \tag{30}$$

where x is the distance in millimeters between the two known points, and pix_{x1} and pix_{x2} are the x-coordinates of the pixels corresponding two the points. Given that x = 62.484 mm, pix_{x1} = 270 and pix_{x2} = 42, the relationship between the known values can be represented as Δx = 0.27405 mm / pixel. This relationship is then used to determine the location of the shock front along the x-axis for the series of images. In order to apply Δx to the images, the locations of each of the

shock front in pixel coordinates had to first be determined. Each of the images were converted to single precision data and preprocessed to ensure no false detection of a wave. This data was used to determine the mean light intensity of the background of the images as well as that of the shock front. The images were evaluated along the negative x-axis to determine the exact pixel coordinates of the front. The locations were then plotted over the images and printed.

It is worth noting that this method resulted in flipped images from the previous series, so the flow direction is towards the left. Additionally, in order to gain a greater resolution to capture the shock front, a smaller frame rate of 10K FPS was required. The resulting series are shown in Figure 11.

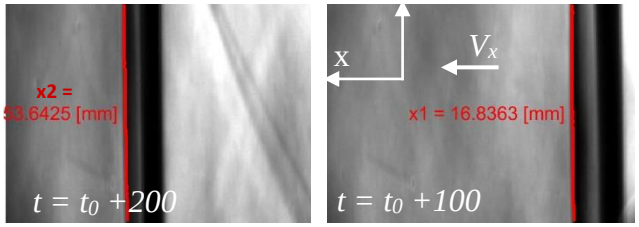

A.

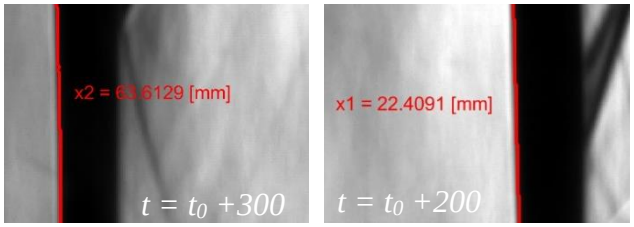

B.

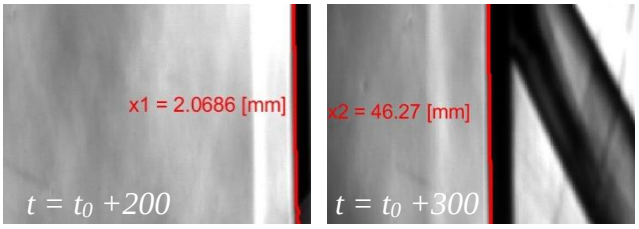

C.

FIGURE 11: Schlieren image wavefront tracking for **A.** 0.003 in, **B.** 0.005 in, and **C.** 0.010 in mylar membrane ruptures.

From the above series, velocity information can be extracted. The shock front velocities as a function of peak overpressure are plotted in Figure 12. While the tracking of the shock front is useful, the velocity may be simply determined by the analytic expressions.

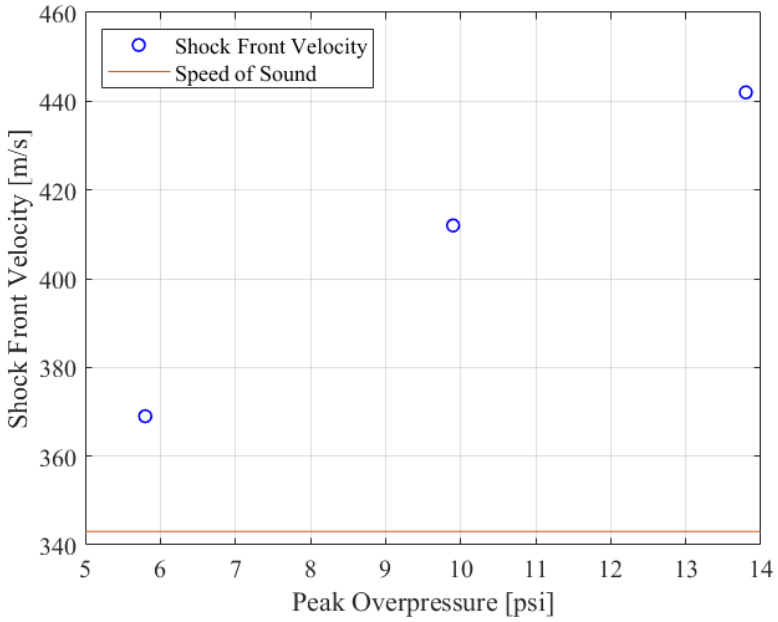

FIGURE 12: Shock front velocity as a function of overpressure.

The above figure does not contain information for the full range of overpressure values. The minor study was conducted to determine the abilities of extracting quantitative data from the

Schlieren series. However, for further trials, Schlieren imaging may not be used, and it is still possible to extract velocity information from the overpressure data.

CHAPTER IV. BLAST/SHOCK-AIRFOIL INTERACTION

A. Schlieren imaging of shock-airfoil interaction

In the present study, A NACA 0012 airfoil/wing model was fabricated and securely mounted between the two side windows within the test section of the blast chamber. The wing model was made of a carbon fiber composite material and manufactured by using a rapid prototyping machine (i.e., 3-D printing) that builds 3-D models layer-by-layer with a resolution of about 25 microns. As shown in Figure 13, the wing model has a chord length of c = 101.6 mm, which spanned the width of the test section. Supported by three stainless-steel rods, the wing model is securely mounted and oriented horizontally across the middle of the test section. The outside window was designed to allow for the rotation of the airfoil at its third-chord.

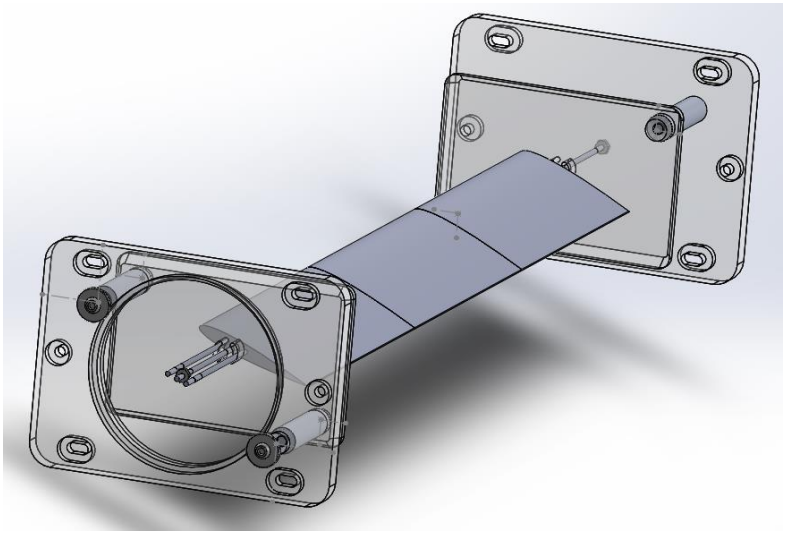

FIGURE 13: The Airfoil/wing model used in the present study.

In order to analyze the interaction between a blast and the airfoil model shown above, the Schlieren imaging system was oriented such that the airfoil was only visible from its cross-section. The ability to rotate the airfoil allows for the investigation of blast interaction across

several angles of attack (AOA) for each overpressure. Figures 14-19 shows the resulting Schlieren image series.

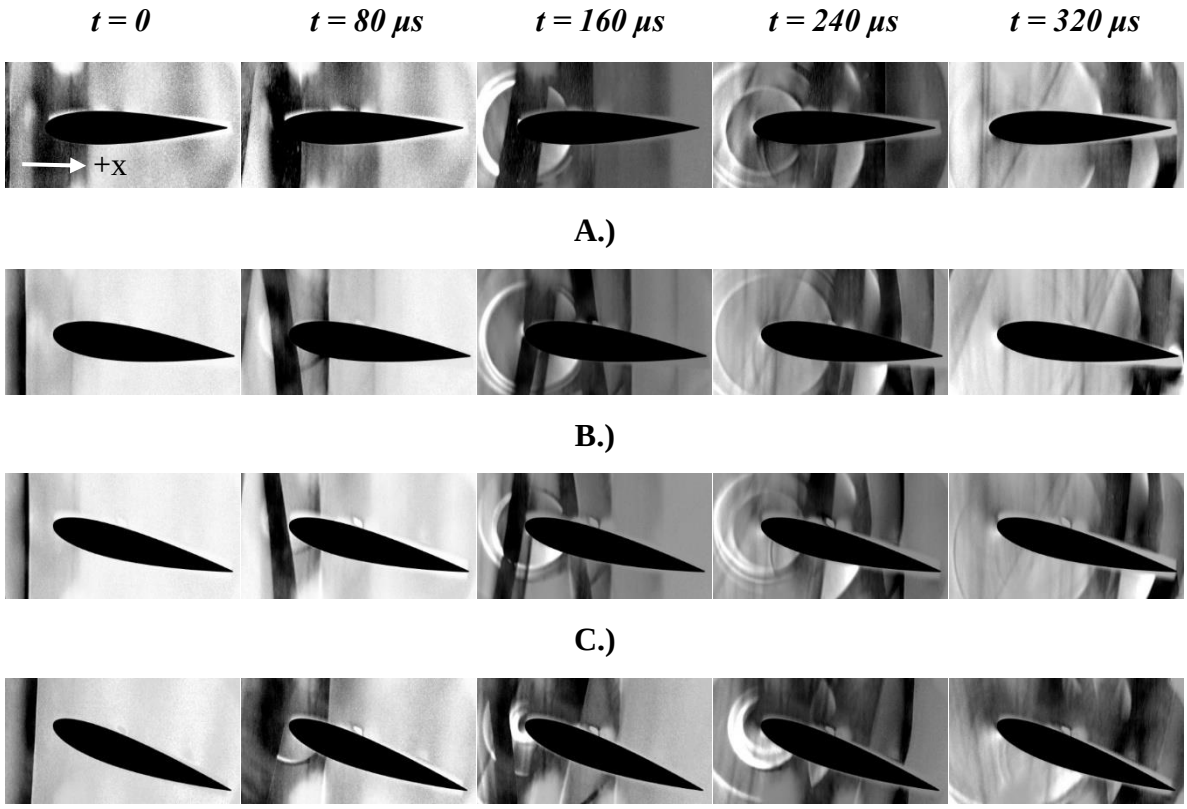

FIGURE 14: Schlieren image series for a 0.002 in mylar membrane rupture for **A**.) 0˚, **B.)** 4˚, **C.)** 8˚, and **D.)** 12˚.

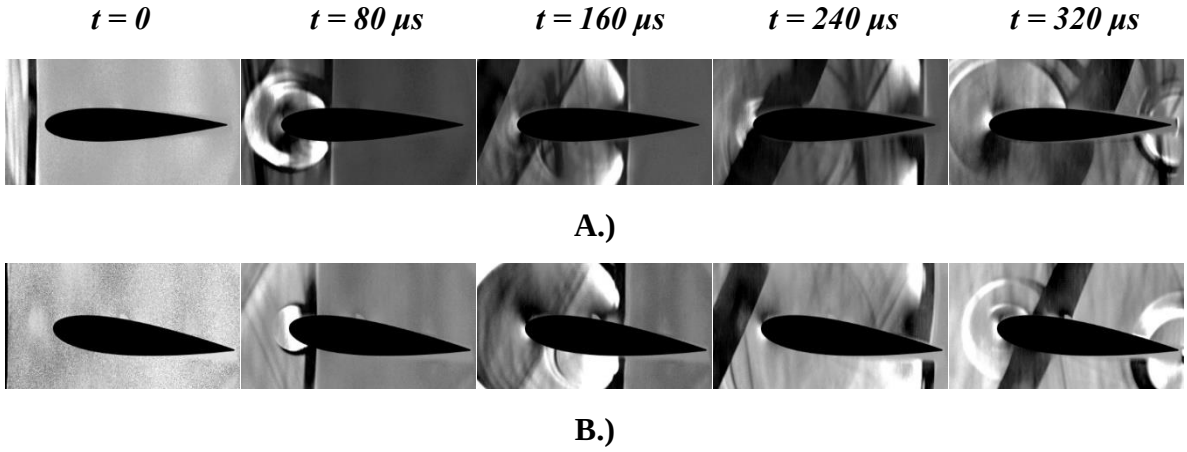

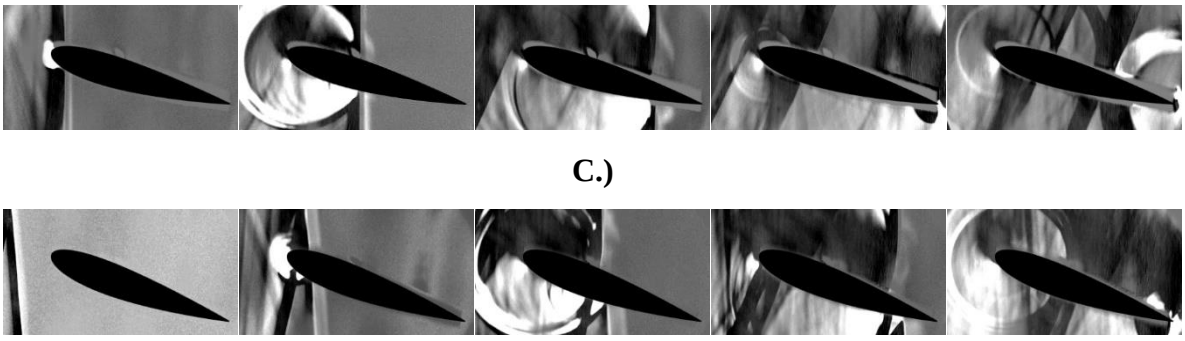

C.)

D.)

FIGURE 15: Schlieren image series for a 0.003 in mylar membrane rupture for **A**.) 0˚, **B.)** 4˚, **C.)** 8˚, and **D.)** 12˚.

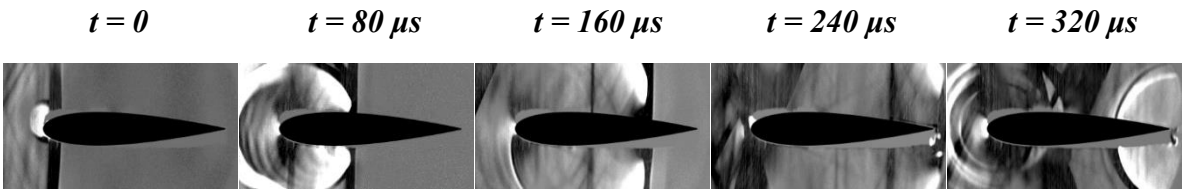

A.)

B.)

C.)

D.)

FIGURE 16: Schlieren image series for a 0.004 in mylar membrane rupture for **A**.) 0˚, **B.)** 4˚, **C.)** 8˚, and **D.)** 12˚.

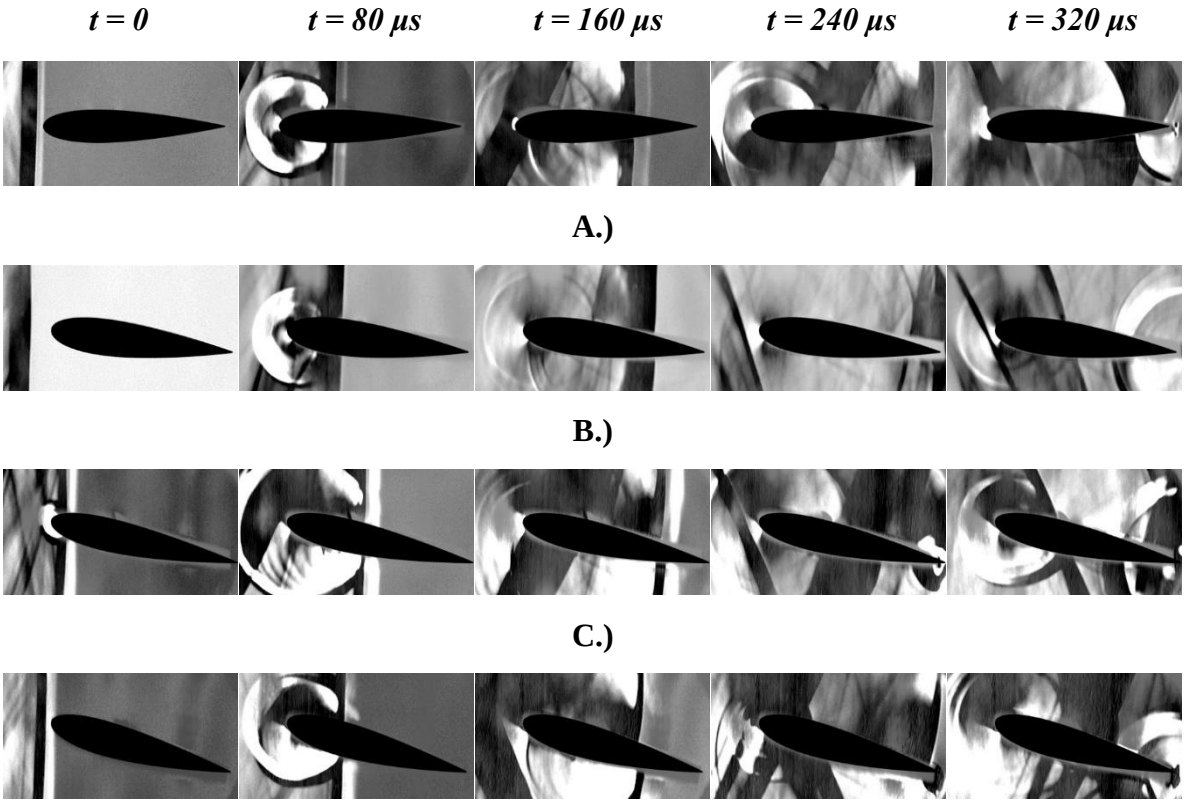

FIGURE 17: Schlieren image series for a 0.005 in mylar membrane rupture for **A**.) 0˚, **B.)** 4˚, **C.)** 8˚, and **D.)** 12˚.

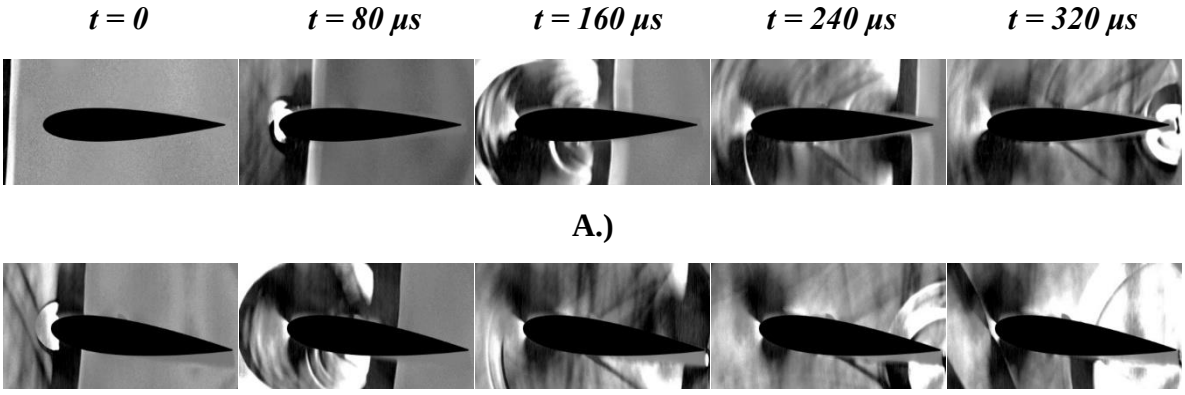

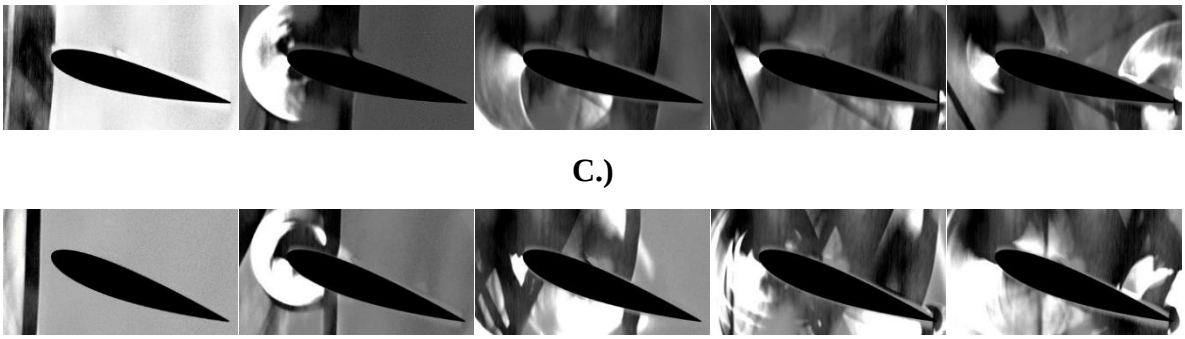

C.)

D.)

FIGURE 18: Schlieren image series for a 0.007 in mylar membrane rupture for **A**.) 0˚, **B.)** 4˚, **C.)** 8˚, and **D.)** 12˚.

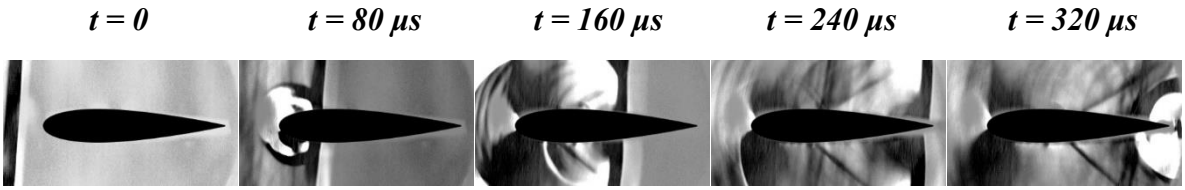

A.)

B.)

C.)

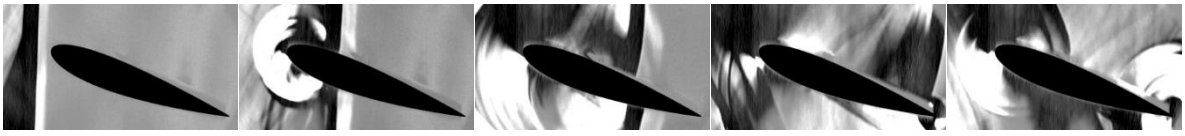

D.)

FIGURE 19: Schlieren image series for a 0.010 in mylar membrane rupture for **A**.) 0˚, **B.)** 4˚, **C.)** 8˚, and **D.)** 12˚.

As shown in the above image series as well as the preliminary image series, as the membrane thickness increases, as does the shock front definition and resulting turbulence. This increase in shock definition can also be seen in the shock reflections. As previously mentioned, the reflected overpressure is a function of the surface the blast encounters. As a result, the initial reflection for the above series appears circular. Because the leading edge of the airfoil is rounded, the reflected blast is as well. As the blasts increase in pressure, this reflection can be seen with greater clarity. Additionally, multiple reflections can be circularly propagating from the leading edge as the pressure increases. It is worth noting that 3-dimensionally, these reflections are cylindrical. Furthermore, the displayed image series are an integration of the entire flow-structure interaction from window to window.

As the blast travels the chord length of the airfoil, an additional reflection can be seen at the trailing edge. The blast/shock is separated at the leading edge of the airfoil, and it is rejoined at the trailing edge. The blast encountering itself combined with the sharp trailing edge of the airfoil results in an additional circular reflection. While the time series shown above are short, the reflection from the leading edge and trailing edge eventually encounter one another, resulting in an even more complex flow.

B. Aerodynamic force measurement of shock-airfoil interaction

While useful information was extracted from the Schlieren image series, quantitative data is necessary to determine the aerodynamic impact of the blast on the airfoil. In an attempt to accurately measure the changes in aerodynamic forces of the airfoil/wing model resulting from the impact of blast waves, a temporally-resolved high-accuracy force/moment sensing system was developed as shown in Figure 20. Two ATI Mini45 force/moment transducers were connected to the two ends of the wing model and securely mounted outside of the side windows

of the blast chamber. The force/moment transducers are composed of foil strain gage bridges, which can measure the forces on three orthogonal axes, and the moment (torque) about each axis. The precision of the force-moment transducers for force measurements is ± 0.25% of the full range (40 N). During the experiments, the force/moment transducers were synchronized via a 16-bit data acquisition system (NI USB-6218) for the data acquisition with a maximum sampling rate of 37,500 Hz. The measurement results of the force/moment transducers were used to determine the aerodynamic responses of the wing model in terms of the lift and drag coefficients (i.e., C_L and C_D).

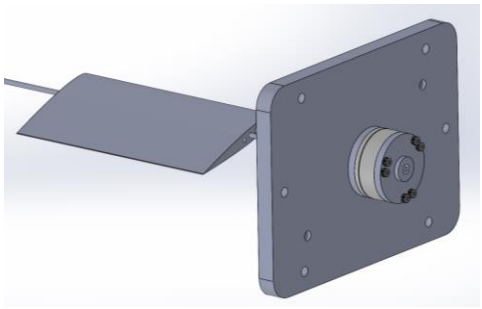

FIGURE 20: Airfoil mounting system for force/moment measurement.

Typically, when using such a force/moment transducer, the calibration, biasing, transformation, and temperature considerations should be taken care of. The data flow used to fully process the force/moment time histories from each trial is shown below:

$$\begin{pmatrix} \text{ST G0} \\ \text{ST G1} \\ \text{ST G2} \\ \text{ST G3} \\ \text{ST G4} \\ \text{ST G5} \end{pmatrix} - \begin{pmatrix} \text{bias0} \\ \text{bias1} \\ \text{bias2} \\ \text{bias3} \\ \text{bias4} \\ \text{bias5} \end{pmatrix} = \begin{pmatrix} \text{bST G0} \\ \text{bST G1} \\ \text{bST G2} \\ \text{bST G3} \\ \text{bST G4} \\ \text{bST G5} \end{pmatrix}$$

A.) **B.)** **C.)**

$$\begin{bmatrix} FxG0 & FxG1 & FxG2 & FxG3 & FxG4 & FxG5 \\ FyG0 & FyG1 & FyG2 & FyG3 & FyG4 & FyG5 \\ FzG0 & FzG1 & FzG2 & FzG3 & FzG4 & FzG5 \\ TxG0 & TxG1 & TxG2 & TxG3 & TxG4 & TxG5 \\ TyG0 & TyG1 & TyG2 & TyG3 & TyG4 & TyG5 \\ TzG0 & TzG1 & TzG2 & TzG3 & TzG4 & TzG5 \end{bmatrix} \times \begin{bmatrix} 1 & 0 & 0 & 0 & 0 & 0 \\ 0 & 1 & 0 & 0 & 0 & 0 \\ 0 & 0 & 1 & 0 & 0 & 0 \\ 0 & 0 & 0 & 1 & 0 & 0 \\ 0 & 0 & 0 & 0 & 1 & 0 \\ 0 & 0 & 0 & 0 & 0 & 1 \end{bmatrix} = \begin{bmatrix} \mathbf{FxG0} & \mathbf{FxG1} & \mathbf{FxG2} & \mathbf{FxG3} & \mathbf{FxG4} & \mathbf{FxG5} \\ \mathbf{FyG0} & \mathbf{FyG1} & \mathbf{FyG2} & \mathbf{FyG3} & \mathbf{FyG4} & \mathbf{FyG5} \\ \mathbf{FzG0} & \mathbf{FzG1} & \mathbf{FzG2} & \mathbf{FzG3} & \mathbf{FzG4} & \mathbf{FzG5} \\ \mathbf{TxG0} & \mathbf{TxG1} & \mathbf{TxG2} & \mathbf{TxG3} & \mathbf{TxG4} & \mathbf{TxG5} \\ \mathbf{TyG0} & \mathbf{TyG1} & \mathbf{TyG2} & \mathbf{TyG3} & \mathbf{TyG4} & \mathbf{TyG5} \\ \mathbf{TzG0} & \mathbf{TzG1} & \mathbf{TzG2} & \mathbf{TzG3} & \mathbf{TzG4} & \mathbf{TzG5} \end{bmatrix}$$

D.) **E.)** **F.)**

$$\begin{Bmatrix} \boldsymbol{Fx} \\ \boldsymbol{Fy} \\ \boldsymbol{Fz} \\ \boldsymbol{Tx} \\ \boldsymbol{Ty} \\ \boldsymbol{Tz} \end{Bmatrix} = \left(\begin{bmatrix} \mathbf{FxG0} & \mathbf{FxG1} & \mathbf{FxG2} & \mathbf{FxG3} & \mathbf{FxG4} & \mathbf{FxG5} \\ \mathbf{FyG0} & \mathbf{FyG1} & \mathbf{FyG2} & \mathbf{FyG3} & \mathbf{FyG4} & \mathbf{FyG5} \\ \mathbf{FzG0} & \mathbf{FzG1} & \mathbf{FzG2} & \mathbf{FzG3} & \mathbf{FzG4} & \mathbf{FzG5} \\ \mathbf{TxG0} & \mathbf{TxG1} & \mathbf{TxG2} & \mathbf{TxG3} & \mathbf{TxG4} & \mathbf{TxG5} \\ \mathbf{TyG0} & \mathbf{TyG1} & \mathbf{TyG2} & \mathbf{TyG3} & \mathbf{TyG4} & \mathbf{TyG5} \\ \mathbf{TzG0} & \mathbf{TzG1} & \mathbf{TzG2} & \mathbf{TzG3} & \mathbf{TzG4} & \mathbf{TzG5} \end{bmatrix} \times \begin{pmatrix} bST\ G0 \\ bST\ G1 \\ bST\ G2 \\ bST\ G3 \\ bST\ G4 \\ bST\ G5 \end{pmatrix}^{T} \right)^{T}$$

G.) **F.)** **C.)**

The rotation matrix is set as an identity matrix, meaning no rotation is considered. When rotations about various axes are to be considered, a standard rotation matrix may be used. For such transformations, it is important to first consider rotations about the axes in the proper order: about the x-axis, then the y-axis, and lastly, the z-axis. For the experimental setup described here, rotations about the x and z axes were used in order to orient the positive x-axis along the length of the blast chamber towards the oncoming blast, the +y-axis upwards, and the +z-axis spanning the length of the wing. Once the data from each of the transducers had been properly calibrated and oriented, the individual sensor data was added to generate the full response of the wing.

There are several considerations to be made regarding the force/moment data being generated here. First, a typical airfoil would be represented as a cantilever, whereas the experimental setup used here has the airfoil fixed at both ends. Because the force generated by a high-pressure blast can potentially damage both the airfoil and the transducers, it was important to securely mount the airfoil from both ends. Additionally, prior to being exposed to the blast wave, the airfoil is not experiencing a nominal flow. The Aerodynamic properties measured here are measured with respect to a stationary state.

In order to measure the lift and drag experienced by the airfoil when encountering a blast, the force/moment measurement system was used. The force transducers were oriented such that the x axis is in the direction of the flow and the y axis is upward. Thus, the drag and lift forces are measured in the x and y directions, respectively. Similar to the pressure measurements, the forces are recorded over time, with the maximum force values being the parameters of interest. For each membrane thickness and angle of attack, five trials were conducted. In order to determine the effects of each blast on the aerodynamic properties of the airfoil/wing model, the lift and drag forces are collected for each trial. The raw forces are then represented by drag and lift coefficients given by Equations 31 and 32, respectively.

$$C_d = (2F_d)/(\rho U^2 A) \tag{31}$$

$$C_L = (2F_L)/(\rho U^2 A) \tag{32}$$

where F_d is the drag force, F_L is the lift force, ρ is the density of air, u is the flow velocity and A is the reference area. Here, the velocity, U, is given by Equation 20. The magnitude of the shock velocity is being used for the fluid velocity because it corresponds to the fluid motion around the airfoil at the instantaneous point the maximum force is observed. Figure 21 shows individual sample C_d and C_L time histories for a 0.003 in membrane thickness at a 0˚ angle of attack.

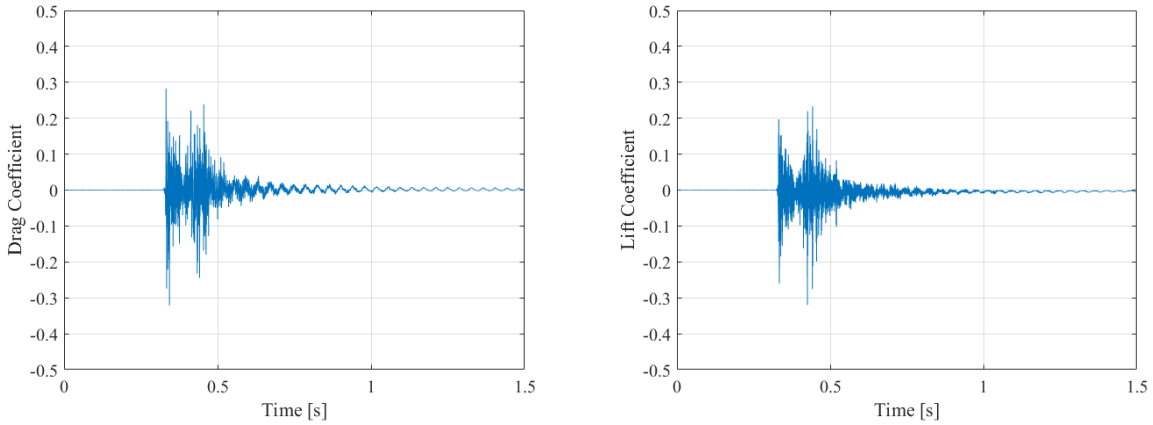

A. **B.**

FIGURE 21: A.) Drag and **B.)** lift coefficient time histories for the rupture of a 0.003 in mylar membrane.

Time histories for each of the membrane thicknesses and angles of attack were recorded and the maximum lift and drag coefficients were recorded for each trial. The drag coefficients plotted as a function of overpressure are shown in Figure 22.

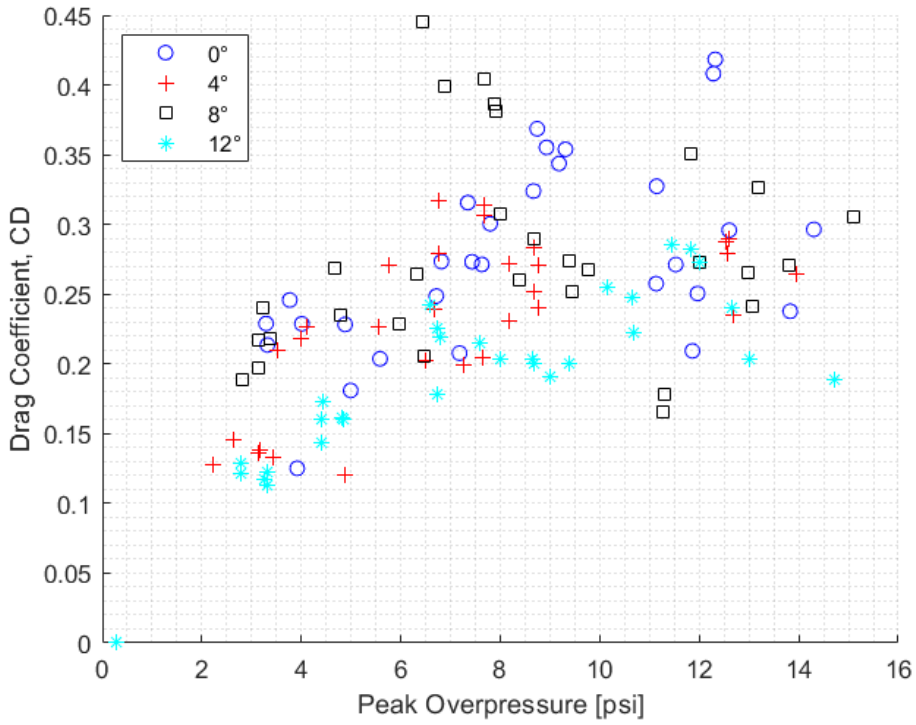

FIGURE 22: Drag coefficient plotted as a function of overpressure for each membrane thickness and airfoil angle of attack.

The above figure shows five trials for each membrane thickness and angle of attack. For each trial, the peak overpressure and maximum drag value was recorded. Here, there is minimal relationship between the overpressures and the corresponding drag coefficients. Additionally, there appears to be little to no relationship between the angle of attack and the drag. For each individual series, there appears to be a maximum drag coefficient. In general, aerodynamic drag is comprised of pressure and friction components. In general, drag in supersonic flows is largely dominated by the pressure component. Here, the lack of dependence of drag on overpressure (and the induced flow velocity) indicates that the drag is dominated by friction. In this case, the blast wave encountering the airfoil results in a rapid development of boundary layer on the surface of the airfoil that results in a friction-dominant drag.

One other proposed reason for the lack of pressure dependence was that the maximum overpressure may not occur at the same time the maximum drag coefficient is observed. This will later be disproven by the good correlation between the overpressure and maximum lift coefficient. This disproves the proposed argument because the maximum lift and drag are observed at the same instant, and there is good linear relationship between the overpressure and lift coefficient. Figure 23 displays this relationship.

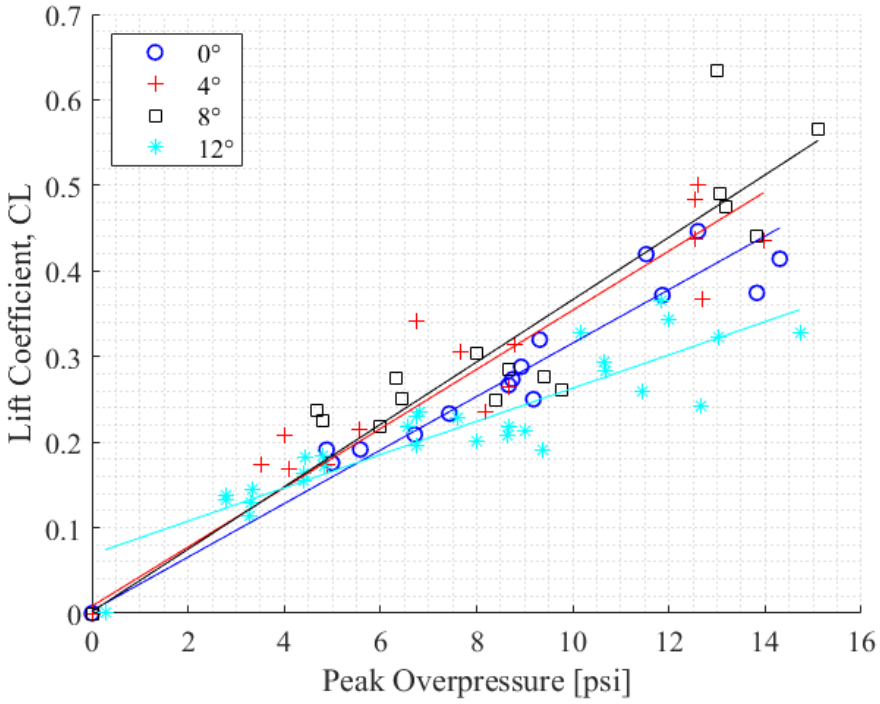

FIGURE 23: Lift coefficient as a function of peak overpressure for each membrane thickness and airfoil angle of attack.

Initially, we can see a good linear relationship between the maximum lift coefficient and the maximum overpressure for each angle of attack. The following table displays the results of linear regression for each angle of attack.

TABLE 4: Linear Regression for C_L as a function of ΔP.

AOA (˚)	R^2	Regression Line
0	0.9903	y = 0.0313x + 0.0031
4	0.9789	y = 0.0346x + 0.0083
8	0.9750	y = 0.0365x + 0.0020
12	0.9020	y = 0.0194x + 0.0688

The linear regression used here does not provide a relationship between the angle of attack and C_L. However, for each separate series, there is a good linear relationship between C_L and ΔP. The minimum correlation coefficient here is 0.9020 for the 12˚ angle of attack and the maximum is 0.9903 for the 0˚ angle of attack. For the 0-8˚ angles of attack, an increase in the slope of the regression line is observed. Upon reaching 12˚ angle of attack, the slope of the regression line does not follow the same trend. The decrease in correlation coefficient along with the lack of agreement with the other angles of attack indicates that a stall is occurring for the 12˚ angle of attack configuration. Upon stalling, the results become less repeatable.

CHAPTER V. CONCLUSION

This work initially shows the capability of the ECU-ABWS to produce repeatable overpressure values in a safe environment. The ABWS was then fitted with a high-speed Schlieren imaging system, allowing for the visualization of blast waves for the first time at this facility. The Schlieren system produced density gradient images of each blast, which indicated that the shock front definition and turbulence increase with blast overpressure.

Following the full characterization of the ABWS, the interaction between a NACA 0012 airfoil and blasts/shocks was investigated. This flow-structure interaction between the blast/shock and the airfoil was visualized using the aforementioned Schlieren imaging system. Cylindrical reflections at both the leading and trailing edges of the airfoil were captured. In addition to the visualization of this process, force measurements were taken in an attempt to represent the aerodynamic impact a blast/shock has on an airfoil. There was little relationship found between the drag coefficient of the airfoil and the respective blast overpressure. The lack of pressure dependence here indicated that the aerodynamic drag is dominated by the friction due to the boundary layer formation resulting from the blast-structure interaction. Alternately, a strong linear relationship was found between the airfoil lift coefficient and the blast overpressure. As the angle of attack increased up to 8˚, the slopes of the regression lines did as well. At the 12˚ angle of attack, the poor correlation indicated a stall.

The capability to visualize and measure the impacts of blasts in the ABWS lends itself to several more research avenues. First, an investigation of blast mitigation techniques will be conducted. There are a variety of materials that have been shown to reduce blast loading and deformation, namely polyurea. The airfoil will be coated with a similar material and the

mitigation efficacy will be conducted. One other mitigation technique of interest is the use of water droplet clouds. This multi-phase fluid-structure interaction is highly complex and basis for the governing physics has been provided.

This work has provided a full investigation of the ABWS and the interaction between blasts/shocks and a NACA 0012 airfoil. In doing so, several more research directions have become available at this facility. The flow-structure interaction visualization method developed for the ECU ABWS allows for the investigation of blast mitigation techniques that may be used for future designs. Furthermore, this system is capable of effectively characterizing the complex multi-phase flow interaction between droplets and shocks, which would further the fundamental knowledge required to develop supersonic and hypersonic vehicles.

REFERENCES

[1] Gan, J., Watanabe, T., Himeno, T., "Effect of Shock Wave Behavior on Unsteady Aerodynamic Characteristics of Oscillating Transonic Compressor Cascade." *Journal of Engineering for Gas Turbines and Power,* 2022, Vol. 144

[2] Guha, A., "A unified theory of aerodynamic and condensation shock waves in vapor-droplet flows with or without a carrier gas," *Physics of Fluids,* 1994, Vol. 6.

[3] Leontiev, A.I., Osiptsov, A.N. Rybdylova, O.D., "The Boundary Layer on a Flat Plate in a Supersonic Gas Droplet Flow: Influence of Evaporating Droplets on the Temperature of an Adiabatic Wall," *High Temperature,* 2015, Vol. 53.

[4] Gebel, G., Mosbach, T., Meier, W., et al, "An Experimental Investigation of Kerosene Droplet Breakup by Laser-Induced Blast Waves," *Journal of Engineering for Gas Turbines and Power,* 2013, Vol. 135

[5] Sharma, S., Singh, A.P., Rao, S.S., et al., "Shock induced aerobreakup of a droplet," Journal of Fluid Mechanics, 2021, Vol. 929.

[6] Anderson, M., Vorobieff, P., Truman, C.R., et al., "An experimental and numerical study of shock interaction with a gas column seeded with droplets," Shock Waves, 2015, Vol. 25, pp. 107-125.

[7] Theofanous, T.G., "Aerobreakup of Newtonian and Viscoelastic Liquids," Annual Review of Fluid Mechanics, 2011, Vol. 43, pp. 661-690

[8] Wells, G.L. "Major Hazards and Their Management," *Institution of Chemical Engineers,* 1997

[9] Tijtgat, N., Volckaert, B., De Turck, F. “Real-Time Hazard Symbol Detection and Localization Using UAV Imagery,” *IEEE 86th Vehicular Technology Conference*, 2017.

[10] Scalea, J.R., Restaino, S., Scasser, M., et al. “The Final Frontier? Exploring Organ Transportation by Drone.” *American Journal of Transplantation*, 2019, Vol. 19, pp. 962-964.

[11] Amukele, T., Ness, P.M., Tobian, A.R., et al. “Drone Transportation of Blood Products,” *Transfusion Practice*, 2017, Vol 57, pp. 582-588.

[12] Sepulveda, E., Smith, H., “Technology challenges of stealth unmanned combat aerial vehicles,” *The Aeronautical Journal*, 2017, Vol. 121, pp. 1261-1295.

[13] Global Security, “Unmanned Aerial Vehicles (UAVs) classes,” *Unmanned Systems Integrated Roadmap*, Department of Defense, 2009.

[14] Larsson, J., Bermejo-Moreno, I., Lele, S.J., “Reynolds and Mach Number effects in canonical shock-turbulence interaction,” *Journal of Fluid Mechanics*, 2013, Vol. 717, pp. 293-321

[15] Rispoli, F., Delibre, G., Venturini, P, et al., “Particle tracking and particle–shock interaction in compressible-flow computations with the V-SGS stabilization and YZβ shock-capturing,” *Computational Mechanics*, 2015, Vol. 55, pp. 1201-1209

[16] Sethuraman, Y.P.M., Sinha, K., Larsson, J., “Thermodynamic fluctuations in canonical shock–turbulence interaction: effect of shock strength,” *Theoretical and Computational Fluid Dynamics*, 2018, Vol. 32, pp. 629-654

[17] Livescu, D., Ryu, J., “Vorticity dynamics after the shock–turbulence interaction,” *Shock Waves,* 2016, Vol. 26, pp. 241-251

[18] Yang, Z., Zhu, Y., “Numerical Investigation of Weak Planar Shock—Elliptical Light Gas Bubble Interaction in Shock and Reshock Accelerated Flow,” *Journal of Fluid Dynamics,* 2021, Vol. 56, pp. 393-402

[19] Xiang, G., Wang, C., Teng, H., Jiang, Z., “Shock/shock interactions between bodies and wings,” *Chinese Journal of Aeronautics,* 2018, Vol. 31, pp. 255-261

[20] Khan, A., Verma, S., Hankare, P., et al., “Shock–shock interactions in granular flows,” *Journal of Fluid Mechanics,* 2020, Vol. 884

[21] Laguarda, L., Patterson, J.S., Schrijer, F.F.J, et al., “Experimental investigation of shock–shock interactions with variable inflow Mach number,” *Shock Waves,* 2021, Vol. 31, pp. 457-468

[22] Peng, D., Xie, F., Liu, X., et al., “Experimental study on hypersonic shock–body interaction between bodies in close proximity using translucent fast pressure- and temperature-sensitive paints,” *Experiments in Fluids,* 2020, Vol. 61.

[23] Ou, J., Ding, J, Luo, X., Zhai, Z., “Effects of Atwood number on shock focusing in shock–cylinder interaction,” *Experimental Methods and their Applications to Fluid Flow,* 2018, Vol. 59

[24] Wu, N, Wang, W., Tian, Y., et al. “Low-cost rapid miniature optical pressure sensors for blast wave measurements,” Optics Express, 2011, Vol. 19 pp. 10797-10804.

[25] Zou, X., Wu, N., Tian, Y., et al., “Ultrafast Fabry–Perot fiber-optic pressure sensors for multimedia blast event measurements,” Journal of Applied Optics, 2013, Vol. 52, pp. 1248-1254

[26] MacPherson, W.N., Gander, M.J., Barton, J.S., et al. “Blast-pressure measurement with a high-bandwidth fiber optic pressure sensor,” Journal of Measurement Science and Technology, 2000, Vol. 11, pp. 95-102

[27] Rahman, S., Timofeev, E., “Pressure measurements in laboratory-scale blast wave flow fields,” Review of Scientific Instruments, 2007, Vol. 78.

[28] Gan, J., Watanabe, T., Himeno, T., “Effect of Shock Wave Behavior on Unsteady Aerodynamic Characteristics of Oscillating Transonic Compressor Cascade.” Journal of Engineering for Gas Turbines and Power, 2022, Vol. 144

[29] Mizukaki, T., Odagiri, T., Matsumura, T., Wakabayashi, K., “Quantitative flow oriented schlieren,” *Journal of Science and Technology of Energetic Materials,* 2020, Vol. 81, pp. 128-136

[30] Hargather, M.J., “Background-oriented schlieren diagnostics for large-scale explosive testing,” *Shock waves,* 2013, Vol. 23, pp. 529-536

[31] Humble, R.A., Scarano, F., van Oudheusden, B.W., “Particle image velocimetry measurements of a shock wave/turbulent boundary layer interaction” *Experimental Fluids,* 2007, Vol. 43, pp. 173-183

[32] Aure, R., Jacobs, J.W., “Particle image velocimetry study of the shock-induced single mode Richtmyer–Meshkov instability,” *Shock Waves,* 2008, Vol. 18, pp. 161-167

[33] Arakeri, J.H., Das, D., Krothapalli, A., et al. “Vortex ring formation at the open end of a shock tube: A particle image velocimetry study,” Physics of Fluids, 2004, Vol. 16, pp. 1008-1019

[34] Needham, C.E., “Simulation Techniques,” in *Blast Waves,* 1st ed. Heidelberg, Germany: Springer, 2010, pp. 293-302.

[35] Hall, T., Holden, J. R., “Navy Explosive Handbook, Explosion Effects and Properties Part III,” *Naval Surface Warfare Center*, Research and Technology Department, 1988.

[36] Martin, J.E., Saul, V., Novick, D., Allen, D. “Assessing the Vulnerability of Unmanned Aircraft Systems to Directed Acoustic Energy,” *Sandia Report,* 2019, Sandia National Laboratories, Albuquerque, NM, USA.

[37] Needham, C.E., “Some Basic Air Blast Definitions,” in *Blast Waves,* 1st ed. Heidelberg, Germany: Springer, 2010, pp. 5-6.

[38] Anderson, J.D, “One-Dimensional Flow,” in *Modern Compressible Flow with Historical Perspective,* 3rd ed. New York, NY, USA: McGraw Hill, 2003, pp. 77.

[39] Anderson, J.D, “Unsteady Wave Motion,” in *Modern Compressible Flow with Historical Perspective,* 3rd ed. New York, NY, USA: McGraw Hill, 2003, pp. 265.

[40] Needham, C.E., “The Rankine-Hugoniot Relations,” in *Blast Waves,* 1st ed. Heidelberg, Germany: Springer, 2010, pp. 9-15.

[41] Needham, C.E., “Blast Wave Reflections,” in *Blast Waves,* 1st ed. Heidelberg, Germany: Springer, 2010, pp. 171-199.

[42] Needham, C.E., “Structure Interactions,” in *Blast Waves*, 1st ed. Heidelberg, Germany: Springer, 2010, pp. 247-269.

[43] Gudmundsson, S., “Aircraft Drag Analysis,” in *General Aviation Aircraft Design, Applied Methods and Procedures*, Butterworth-Heinemann, 2014, pp. 661-760.

[44] Vinogradov, Y.A., Zditovets, A.G., Kiselev, N.A., et al., “Measurement of the Adiabatic Wall Temperature of a Flat Plate in a Supersonic Air-Droplet Flow,” *Fluid Dynamics*, 2020, Vol. 55, pp. 701-707.

[45] Sharma, S., Singh, A.P., Rao, S.S., et al., “Shock induced aerobreakup of a droplet,” *Journal of Fluid Mechanics*, 2021, Vol. 929.

[46] Chen, Y., DeMauro, E.P., Wagner, J.L., et al., “Aerodynamic Breakup and Secondary Drop Formation for a Liquid Metal Column in a Shock-Induced Cross-Flow,” *Sandia National Laboratories*, 2016

[47] Syer, J., Ryan, T.J. “Toward Tuning Blast Parameters in a Blast Simulator for Improved Injury Research Capability,” BMES, 2018. Greenville, NC, USA. Poster. Department of Engineering, East Carolina University

[48] Kailasanath, K., Tatem, P.A., Williams, F.W., Mawhinney, “Blast Mitigation Using Water – A Status Report,” 2002, *Naval Research Laboratory*, Washington, DC.

[49] Teich, M., Gebbeken, N., “Structures Subjected to Low-Level Blast Loads: Analysis of Aerodynamic Damping and Fluid-Structure Interaction,” 2012, *Journal of Structural Engineering*, Vol. 138, pp. 625-635

[50] Nyein, M.K., Jason, A.M., Yu, L., et al., “In silico investigation of intracranial blast mitigation with relevance to military combat traumatic brain injury,” 2010, *Biophysics and Computational Biology*, Vol. 107, pp. 20703-20708.

[51] Grujicic, M., Bell, W.C., Pandurangan, B., Glomski, P.S., “Fluid/Structure Interaction Computational Investigation of Blast-Wave Mitigation Efficacy of the Advanced Combat Helmet,” 2011, *Journal of Materials Engineering and Performance*, Vol. 20, pp. 877-893.

[52] Bartyczak, S., Mock, W., “Characterization of viscoelastic materials for low-magnitude blast mitigation,” 2014, *Journal of Physics: Conference Series*, 500.

[53] Iqbal, N., Tripathi, M., Parthasarathy, S., “Polyurea coatings for enhanced blast-mitigation: a review,” 2016, *The Royal Society of Chemistry: RSC Advances*, Vol. 6, pp. 109706-109717.

[54] Igra, O., Falcovitz, J., Houas, J., Jourdan, G., “Review of methods to attenuate shock/blast waves,” 2013, *Progress in Aerospace Sciences*, Vol. 58, pp. 1-35.

[55] Jourdan, G., Biamino, L., Mariani, C., et al., “Attenuation of a shock wave passing through a cloud of water droplets,” 2009, *Shock Waves*, Vol. 20, pp. 285-296